Perovskite-related ReO_3-type structures

Hayden A. Evans[1,2]*, *Yue Wu*[3], *Ram Seshadri*[1,4,5] *and Anthony K. Cheetham*[1,5,6]*

Abstract | Materials with the perovskite ABX_3 structure play a major role across materials chemistry and physics as a consequence of their ubiquity and wide range of useful properties. ReO_3-type structures can be described as ABX_3 perovskites in which the A-cation site is unoccupied, giving rise to the general composition BX_3, where B is typically a cation and X is a bridging anion. The chemical diversity of such structures is extensive, ranging from simple oxides and fluorides, such as WO_3 and AlF_3, to complex structures in which the bridging anion is polyatomic, such as in the Prussian blue-related cyanides $Fe(CN)_3$ and $CoPt(CN)_6$. The same ReO_3-type structure is found in metal–organic frameworks, for example, $In(im)_3$ (im = imidazolate) and the well-known MOF-5 structure, where the B-site cation is polyatomic. The extended 3D connectivity and openness of this structure type leads to compounds with interesting and often unusual properties. Notable among these properties are negative thermal expansion (for example, ScF_3), photocatalysis (for example, $CoSn(OH)_6$), thermoelectricity (for example, $CoAs_3$) and superconductivity in a phase that is controversially described as SH_3 with a doubly interpenetrating ReO_3 structure. We present an account of this exciting family of materials and discuss future opportunities in the area.

[1]*Materials Research Laboratory, University of California, Santa Barbara, CA, USA.*

[2]*National Institute of Standards and Technology, Center for Neutron Research, Gaithersburg, MD, USA.*

[3]*Department of Chemistry and Materials Innovation Factory, University of Liverpool, Liverpool, UK.*

[4]*Department of Chemistry and Biochemistry, University of California, Santa Barbara, CA, USA.*

[5]*Materials Department, University of California, Santa Barbara, CA, USA.*

[6]*Department of Materials Science and Engineering, National University of Singapore, Singapore, Singapore.*

**e-mail: hayden.evans@nist.gov; akc30@cam.ac.uk*

https://doi.org/10.1038/s41578-019-0160-x

Recent developments in photovoltaic devices with active layers containing hybrid perovskite halides, such as $(MA)PbI_3$ (MA = methylammonium)[1], have drawn our attention once more to the importance and versatility of perovskite-based materials. These iconic materials, of general formula ABX_3 (FIG. 1a), have a long and distinguished history, with milestones including the discoveries of ferroelectric $BaTiO_3$ (REF.[2]), ferromagnetic $SrRuO_3$ (REF.[3]), superconducting $YBa_2Cu_3O_7$ (REF.[4]), magnetoresistive $(La_xSr_{1-x})MnO_3$ (REF.[5]) and multiferroic $BiMnO_3$ (REF.[6]). Striking breakthroughs in the hybrid perovskite area include the discoveries of ferroelectric and multiferroic behaviour in formates, such as $(DMA)Mn(HCOO)_3$ (DMA = dimethylammonium), where the X anion is an organic linker rather than a simple halide or oxide anion[7], and ferroelectric, metal-free perovskites ((*N*-methyl-*N*′-diazabicyclo[2.2.2] octonium)-ammonium triiodides)[8].

It is often overlooked that the ABX_3 perovskite structure is based on an even simpler structure type in which there are no cations in the A-site cavities. Such BX_3-type structures (where B is typically a metal) are most notably illustrated by the eponymous ReO_3 structure (FIG. 1b,c). This comprises a network of ReO_6 octahedra that share common corners in three dimensions, in this case with an Re–O–Re angle of 180° (although such linear linkages are unusual for most ReO_3-type materials). Recalling that the perovskite family now comprises an extensive range of compounds with both simple and complex X-anion linkers[9], we have begun to explore the extent to which this is also true for ReO_3-type materials. Our article addresses this question, drawing together examples of ReO_3-type phases, ranging from simple oxides and halides, such as WO_3 and ScF_3, to systems containing more complex linkers and nodes, such as the formates $M^{III}(HCOO)_3$ (M = metal), hypophosphites $M^{III}(H_2POO)_3$, imidazolates $M^{III}(C_3N_2H_3)_3$ and borohydrides $Ln(BH_4)_3$ (Ln = lanthanide). We show that this family is far more extensive than has hitherto been recognized, and that the members display a remarkable range of functionality that almost matches that of perovskites. FIGURE 2 illustrates this point, showing the timelines of discoveries and properties of these ReO_3-type materials, as well as their considerable chemical scope. Furthermore, our survey of the literature suggests that there are several chemical families that have yet to be explored.

One characteristic of ReO_3-type structures is their openness, which is immediately apparent when comparing the structure of ReO_3 with the perovskite structure (FIG. 1). This feature is even more striking in expanded ReO_3 structures, such as those in which the X-site has a multiatom linker. Several aspects of the openness influence the structures and properties of ReO_3 materials. In terms of the structures, the openness often results in tilting of the BX_6 octahedra, leading to more stable structures with bent B–X–B linkages[10]. Tilting of octahedra in perovskites has been extensively studied[11–13], including the analysis of group–subgroup relationships, and the concepts in this area have been extended to multiatom X-site linkers[14,15]. These ideas can be applied to ReO_3-type structures, but will not be discussed further here. However, we note that tilting, or the absence of it, can

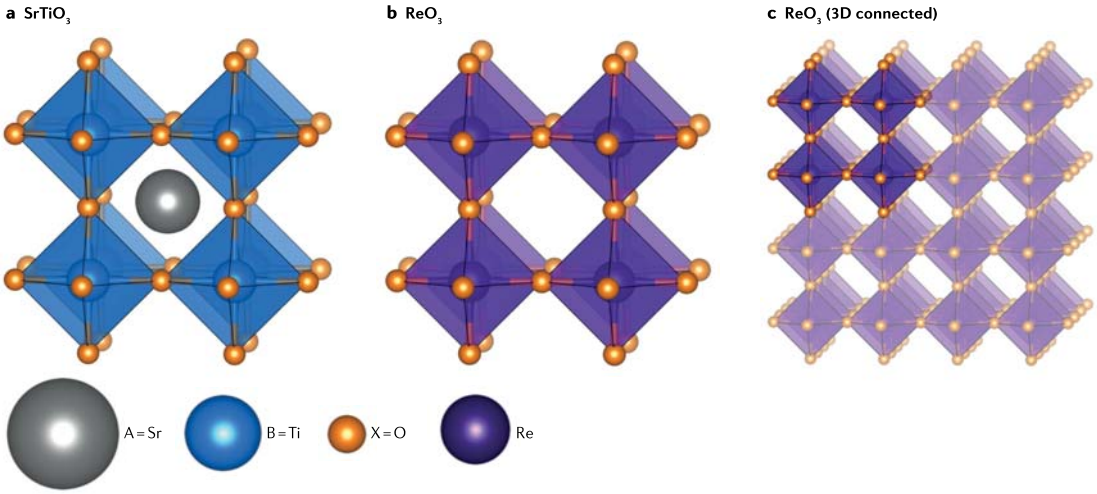

Fig. 1 | **General structures of perovskites and ReO_3. a |** The ABX_3 perovskite structure, exemplified by cubic $SrTiO_3$. **b |** The ReO_3 structure, illustrated by ReO_3 itself, contains no cation on the A-site. It is therefore an array of corner-sharing BX_6 octahedra. Panels **a** and **b** are drawn to scale to remind the reader that the ReO_3 unit cell is smaller because of the smaller size of the Re^{6+} cation. **c |** The ReO_3 structure, drawn to show its extended 3D connectivity. The VESTA software suite was used to create all visualizations of crystal structures in this manuscript[252].

significantly affect electronic and magnetic properties, for example, in ReO_3 itself and some structures with cyanide X-site linkers. Turning to other manifestations of the openness of ReO_3-type structures, cation insertion into the vacant A-site cavity is often facile, both in terms of the availability of space and the ease of ion transport; this has enabled applications in the area of rechargeable batteries. The openness also amplifies the vibrational properties associated with the X-site linkers, which has led to outstanding examples of negative thermal expansion (NTE). Finally, systems with multiatom X-site linkers, where the openness is particularly high, can accommodate guest molecules in the A-site cavities, in some cases leading to interesting adsorption–desorption behaviour.

This Review begins with a focus on simple inorganic compounds, especially the oxides, fluorides and oxyfluorides, and then explores more complex phases with multiatom linkers on the X-site. We note that one requirement for the adoption of the ReO_3-type structure is that the chemistry must be able to support octahedral connectivity at the B-sites. Bearing this in mind, we shall also consider some metal–organic frameworks (MOFs) in which the B-site node is polyatomic, the most striking of which is MOF-5 (REF.[16]).

Inorganic systems

The inorganic ReO_3-type materials are the oldest and most established compounds discussed in this Review. The first documented example is the pigment Prussian blue in the early 1720s, which we know today to belong to this structure type. Of the inorganic ReO_3-type compounds, those with single-atom X^- linkers predominate, with the fluorides being the most numerous. The fluorides are followed in prevalence by the hydroxides, oxyfluorides and intermetallics, and then the oxides and nitrides. Although the cyanides predate all other inorganic ReO_3-type compounds, we prefer to organize this section on inorganic systems based on the date of crystallographic structure determination. We therefore lead with the eponymous ReO_3, and progress accordingly.

Oxides. ReO_3, which is deep red in colour, was first reported in the early 1930s, when its synthesis was described and its structure determined by powder X-ray diffraction[17]. However, it was not until 1965, when Goodenough and co-workers reported that it was a metallic conductor, that it attracted the attention of the scientific community[18]. Oxide conductors were rarities at that time, and the behaviour of ReO_3 was particularly eye-catching because its conductivity was almost as high as that of copper. That finding led to subsequent studies of the electronic structure of ReO_3, which involves band formation from overlap between the rhenium 5*d* (t_{2g}) and oxygen 2*p* (p_x or p_y) orbitals[19]. More than 50 years after the work of Goodenough and co-workers, ReO_3 remains the most striking example of a metallic transition-metal oxide.

ReO_3 and WO_3 are the only binary oxides that crystallize with the ReO_3-type structure, but although structurally similar, their properties are quite different. For example, at room temperature, ReO_3 is pcu (primitive cubic) and conductive, whereas WO_3 is monoclinic and insulating. The difference lies in their contrasting M–O–M bond angles: ReO_3 has angles of 180°, and WO_3 has angles between 165° and 179° (REF.[20]). This distortion is a consequence of the propensity for tungsten atoms to be displaced from the ideal cubic location in the WO_6 octahedral environments, which density functional

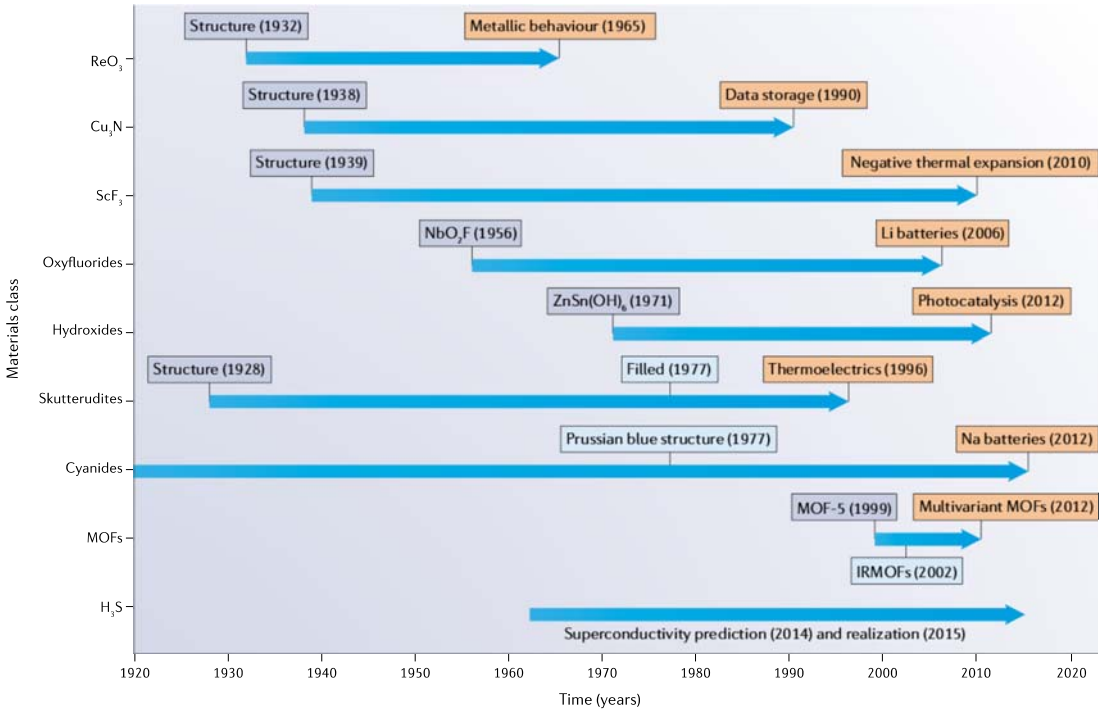

Fig. 2 | **Timeline of ReO_3-type materials.** It is interesting to note the long time period between discoveries and reported properties, as well as the diverse chemical compositions and functionalities of ReO_3-type materials. IRMOF, isoreticular MOF; MOF, metal–organic framework.

theory calculations suggest is caused by non-populated antibonding orbitals in the conduction band. In ReO_3, this is the reverse, as the antibonding orbitals are populated and the tendency to displace is discouraged[21]. This theory has been supported by experiments, because solid solutions of ReO_3 and WO_3 ($Re_xW_{1-x}O_3$) become cubic at an x value of 0.25; this change is also marked by an increase in conductivity[22].

Not only is the cubic ReO_3 structure stable up to its 673 K melting point[23] (in contrast to WO_3, which undergoes multiple first-order phase transitions with temperature), it also displays NTE[23,24] — the phenomenon where a material contracts instead of expanding when heated. This property is useful in composites, where the strain from the positive thermal expansion of one phase can be offset by the NTE of another[25]. Rodriguez et al. described how for ReO_3 samples with high static disorder of oxygen, NTE was diminished[26]. The weakened NTE is a consequence of the oxygen disorder, which alters the state of the antibonding band, reducing the Fermi pressure responsible for the rigidity of the structure. In a more holistic sense, NTE is commonly seen in materials with corner-connected M–X polyhedra that undergo concerted tilting or rocking motions when transverse vibrations (the movement of X species perpendicular to the M–X–M bond) are excited[27]. Famous NTE compounds, such as ZrW_2O_8, Prussian blues and zeolites, all display some form of excited transverse vibrational modes related to their NTE behaviour[27]. We shall see other striking examples of NTE in ReO_3-type systems in some of the following sections.

In addition to exhibiting NTE, ReO_3 displays pressure-induced first-order phase transitions. These pressure-dependent phase transitions (which involve octahedral rotations) occur as a stress relief[28], as the ReO_6 octahedra do not distort easily because of the strong Re–O bonds[29]. These phase transitions have been examined via diffraction experiments[30–32]; however, a pressure phase diagram was only resolved in 2015 with the implementation of high-pressure Raman studies[33]. In addition to physical pressure, chemical pressure in the form of lithiation can induce phase transitions in ReO_3, as was first examined in the 1980s by Cava et al.[34,35], and more recently by Melot and co-workers[36], where considerable correlated rotations of the corner-sharing ReO_6 octahedra are observed upon lithiation.

Lastly, although ReO_3 has generated a large amount of interest, it should not be overlooked that WO_3 is an attractive wide band-gap semiconductor that can be tuned through intercalation, temperature, doping and nanostructuring. In particular, nanostructuring is an attractive strategy to stabilize one of the three other WO_3 phases at room temperature[37] or to increase the surface area for enhanced chemical functionality. For

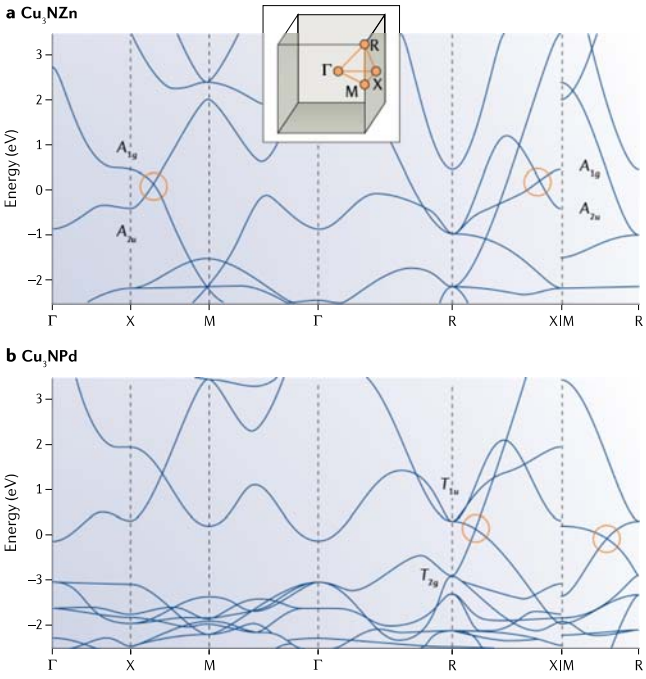

Fig. 3 | **Electronic structures of inverse perovskite nitrides. a |** Electronic structure of Cu_3NZn. **b |** Electronic structure of Cu_3NPd. The orange circles indicate the Dirac points in the band structures of these inversion-symmetric Dirac materials. The inset in panel **a** is a sketch of the Brillouin zone. Adapted with permission from REF.[74], American Physical Society.

example, earlier work on WO_3 for its use as a photochromic[38,39], electrochromic[40], photocatalytic[41], superconductive[42], ferroelectric[43] and gas-sensing[44–47] material is still relevant and continues to inform active areas of research[17]. This includes photoelectrochemical[48–52], photochromic[53], conductive[54], anodic[55], photocatalytic[56–59], thermoelectric[60,61] and gas-sensing[62,63] applications.

One recent work used WO_3 as an electron conductor in a core–shell nanowire $BiVO_4$ photoanode for photoelectrochemical water oxidation[64]. This study was significant because the core–shell nanowire design leveraged the high light absorption of $BiVO_4$, whilst mitigating its low transport properties with WO_3. Another example demonstrated the use of an apoferritin-encapsulated, nanoparticle-coated WO_3 material for sensitive detection of certain molecules in exhaled breath, and thus its great promise for reliable, non-invasive, diagnosis of diseases[62]. Lastly, WO_3 is able to tune the surface charge transfer of diamond, resulting in improved p-type sheet conductivity and thermal stability[65]. In fact, the transfer doping efficiency with WO_3 was the highest (for the given surface area) reported to date, marking a substantial advance in 2D diamond-based electronic devices. This study and earlier work on WO_3 attest to this material's suitability for a wide variety of applications.

Nitrides. The anti-ReO_3 crystal structure of Cu_3N was determined in 1938 by Juza and Hahn[66], not long after the discovery of ReO_3, and has been confirmed in subsequent work[67]. Its crystal structure in space group $Pm\bar{3}m$ is the same as that of ReO_3 because the N–Cu–N bond angles are also 180°. Under high pressure, Cu_3N transforms to a simple tetragonal structure, which is not surprising given the open nature of the structure[68]. There has not been a detailed study of NTE in Cu_3N; however, it has been indicated that there is little, if any, expansion in the temperature range of 4–100 K (REF.[69]). Since its discovery, more than 50 years lapsed before the growth of thin films was reported[70] and attention was drawn to the semiconducting properties of Cu_3N. Shortly thereafter, in 1990, it was shown that such films, which are typically green, could be used as an optical data-recording medium using infrared light[71]. The films were made by irradiating copper with nitrogen ions during film deposition onto a substrate because copper does not react with nitrogen gas (although bulk samples can be made from the reaction between CuF_2 and NH_3)[72]. Since 1990, there has been extensive work on the preparation of high-quality thin films using various methods, especially magnetron sputtering and radio-frequency plasma jets.

In addition to its potential for use in optical data storage, Cu_3N has been proposed as a defect-tolerant semiconductor for photovoltaic applications[73]. Moreover, in condensed matter physics, it has been suggested as a model for a new type of topological semimetal exhibiting Dirac line nodes near the Fermi energy on doping with non-magnetic transition metal atoms, such as zinc and palladium[74] (FIG. 3). For energy storage, Cu_3N has been studied as a cathode material of lithium-ion batteries, although the chemistry is complex and may preclude its adoption by industry[75]. It has also been studied as a cathode for oxygen reduction in alkaline fuel cells[76].

Dark-blue sodium nitride, Na_3N, which is isostructural to Cu_3N, has been prepared by the reaction of metallic sodium or liquid NaK alloy with plasma-activated nitrogen at low pressures[77]. Na_3N decomposes above 377 K into its constituent elements, with a standard enthalpy of formation of approximately +64 kJ mol^{-1} (REF.[78]), making it a rare example of a metastable ReO_3-type structure. The band gap of Na_3N is in the range 0.5–1.0 eV, which is similar to that of Cu_3N. Na_3N shows no phase change down to 20 K, but does exhibit strongly anisotropic effects[79]. There is no tilting of the NNa_6 octahedra, and nor is there any NTE, which is surprising. However, similar to Cu_3N, Na_3N may exhibit topological semimetal behaviour[80]. It is also worth noting that neither Li_3N nor K_3N adopt the anti-ReO_3-type structure[81,82].

Fluorides and oxyfluorides. ReO_3-type fluoride materials, of general formula MF_3, are more common than their oxide counterparts owing to the greater prevalence of 3+ oxidation-state metals. The M-site metals for MF_3 compounds include scandium[83], cobalt[84], aluminium[85], chromium[86], vanadium[87], titanium[88] and iron[86]. It is worth noting that rare-earth cations — even the smallest example of lutetium (ionic radius of 0.861 Å)[89,90] — are too large to adopt the octahedral coordination

required for the ReO_3-type structure. The majority of the single-metal ReO_3-type fluoride compounds adopt a rhombohedral distorted variant structure at room temperature, with the exceptions being ScF_3 — a notable NTE material — and MnF_3, which is Jahn–Teller distorted[83]. As will become apparent throughout this Review, the majority of inorganic ReO_3-type materials have been studied for properties that are exhibited by ReO_3 itself: curious thermal expansion, as a host for guest cations and unusual pressure-dependent structural behaviour. This does not mean, however, that they do not, or cannot, display other attractive properties.

ScF_3 is perhaps the best-known MF_3 compound because it displays a remarkable temperature range of NTE as a consequence of the transverse vibrations of the fluorine anions[91] (FIG. 4a,b depicts ReO_3 behaviour for comparison). From 10 K to approximately 1100 K, the material does not undergo first-order phase transitions, in contrast to ReO_3 (REF.[92]) (although a possible quantum phase transition has been reported)[93], and displays a coefficient of NTE near -8 ppm K^{-1} at room temperature. This coefficient of NTE is comparable to -9 ppm K^{-1} for the well-known NTE compound ZrW_2O_8 (REF.[83]). Furthermore, it was shown that the degree of NTE in ScF_3 is particle size dependent[94], and can be tuned between NTE, zero thermal expansion and positive thermal expansion by nanostructuring the product[95]. The tunability has been ascribed to local symmetry breaking as the particle size is decreased; that is, the local structure is rhombohedrally distorted (as evidenced by pair distribution studies) but appears cubic on average. The source of this local symmetry breaking is thought to be the increased surface pressure from the decreased particle size. This tuning can also be achieved by zirconium doping[96]. In addition, it has been found that NTE in ScF_3 can be turned off by doping with a small amount of iron and intercalating an equal amount of lithium into the vacant A-sites[97]. The inclusion of lithium ions limits the transverse vibrations of the fluoride ions, in much the same way as guest molecules can dampen NTE in other porous NTE materials[98–102].

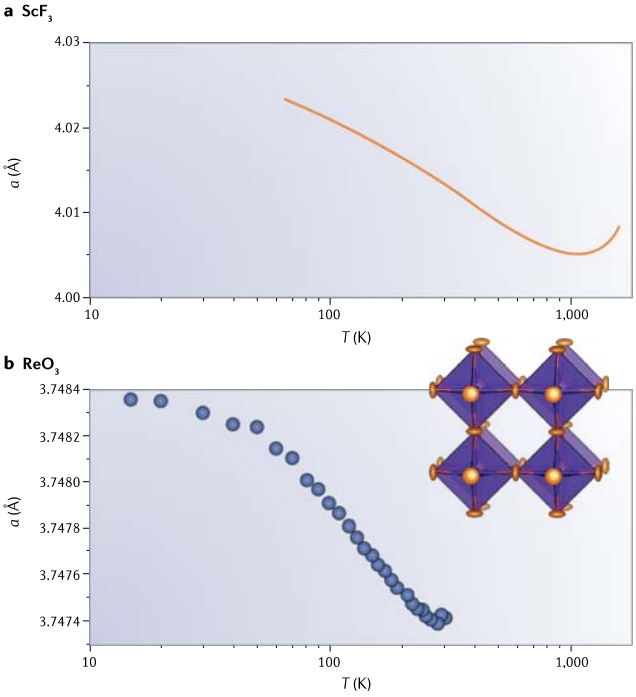

Fig. 4 | **Lattice constant as a function of temperature. a** | The change in lattice constant, *a*, for ScF_3 obtained from a combination of data from synchrotron X-ray diffraction and neutron diffraction. **b** | The change in lattice constant for ReO_3 based on data from neutron diffraction experiments. The cubic ReO_3 structure is shown as an overlay (95% thermal ellipsoids). Note the magnitude of the negative thermal expansion is much greater for ScF_3 than for ReO_3. Panel **a** is adapted with permission from REF.[83], American Chemical Society. Panel **b** is adapted from REF.[76] (Rodriguez, E. E. et al. The role of static disorder in negative thermal expansion in ReO_3. *J. Appl. Phys.* **105**, 114901, 2009), with the permission of AIP Publishing.

Redox-active MF_3 materials that have been examined as intercalation materials for batteries include those where M = Ti, V, Mn, Co or Fe (REFS[103,104]). The predominant focus has been on FeF_3 because it displays the most promising charge–discharge profile, a viable voltage range (2–4 V) and increased thermal stability upon lithiation[105]. However, because of the low electrical conductivity of FeF_3 (and fluorides in general), ball-milling with a conductive carbon to increase electron transport is always needed. In the case of FeF_3, a reversible capacity of 80 mAh g^{-1} is achievable after this process[103]. Aside from conductive carbon additives, nanostructuring FeF_3 to increase the surface area for lithiation[106–110] and doping with cobalt have been studied as ways to increase conductivity. However, theory suggests that FeF_3 becomes less stable with cobalt doping[111] and tends to form a tungsten bronze-related structure, which is a possible battery material in its own right[112]. The tungsten bronze structure is also observed with iron fluoride hydrate, $FeF_3{\cdot}0.33\ H_2O$, and is found to perform in a manner similar to the cobalt-doped compound in battery applications[113]. Lastly, there are reports that the perovskite $NaFeF_3$ can be completely (100%) desodiated and sodiated reversibly, and is of interest for sodium battery cathodes[114].

Double-fluoride ReO_3-type compounds, with the general formula $MM'F_6$, come in many varieties. Examples include $Sn^{2+}Sn^{4+}F_6$ (REF.[115]), $M^{2+}(Zr)F_6$ compounds (where M = Fe (REFS[116,117]), Pd (REF.[118]), Co (REF.[119]), Zn (REF.[119]), Mg (REF.[120]), Cu (REF.[121]), V (REFS[122,123]), Ti (REF.[122]), Ca (REFS[117,124]), Cr (REF.[117])), $M^{2+}(Hf)F_6$ compounds (where M = V, Ti (REF.[122])), $MMoF_6$ compounds (where M = Na (REF.[125]), Cu (REF.[126])), $MNbF_6$ compounds (where M = Cr (REF.[126]), V (REFS[123,127])) and $NaSbF_6$ (REF.[128]). Some of these compounds display NTE[124,129,130], gas adsorption under pressure[124] as well as Jahn–Teller distortions governed by the M^{2+} character[117,121,123]. There are also recent reports of $YbZrF_7$ (REF.[131]), which displays NTE below room temperature and zero thermal expansion at 300 K, and $Mg_{1-x}Zr_{1+x}F_{6+2x}$ compounds in which the degree of thermal expansion can be tuned by varying *x* (REF.[132]).

ReO_3-type oxyfluorides with the general formula MO_xF_y (M = Ti (REF.[133]), V (REF.[134]), Ta (REF.[135]), Nb (REFS[133,135]), Zr (REF.[136]), Mo (REF.[137])) are also known, with the first

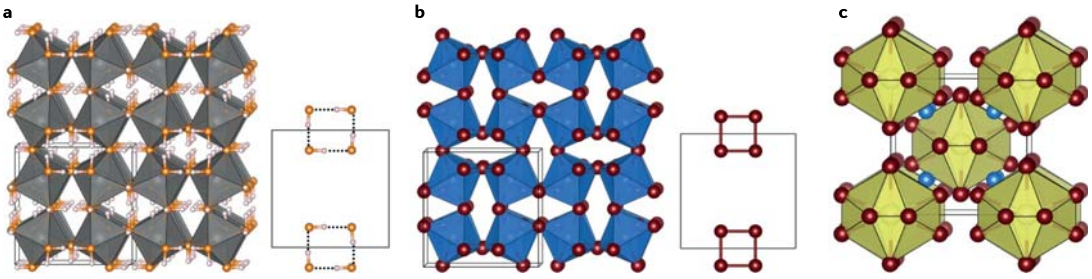

Fig. 5 | **Structural similarities between $In(OH)_3$ and $CoAs_3$. a |** Structure of $In(OH)_3$. **b |** Structure of $CoAs_3$. Panels **a** and **b** are drawn to scale. The bonding between As atoms follows the same motif as the 'ice-rules' hydrogen bonding in $In(OH)_3$. **c |** $CoAs_3$, emphasizing the 12-coordinate cavity, or cage, that can be filled with a cation. This cation 'rattles' inside the cavity, increasing thermoelectric performance via phonon scattering. Atom legend: indium, grey; oxygen, orange; hydrogen, white; cobalt, blue; arsenic, red; and 12-coordinate cavity, yellow.

example reported in the 1950s[135]. They are predominantly tertiary compounds, but there are examples of quaternary compounds, like the non-stoichiometric $Nb_{0.55}Zr_{0.45}O_{1.1}F_{0.8}$ (REF.[136]), $CrNb_2O_4F_5$ and $Fe_2Nb_3O_6F_9$ (REF.[138]), and $MgNb_2O_3F_6$ and $MgTi_2OF_8$ (REF.[139]). ReO_3-type oxyfluorides have been primarily studied as intercalation materials for use in batteries[133,134], with the greater class of oxyfluorides viewed as a favourable middle ground between oxides and fluorides, leveraging the high voltage levels of the fluorides and increased stability of the oxides (owing to the more covalent M–O bonds). As with all battery materials, understanding the underlying crystal chemistry of each compound is important, because the anion and cation orders have a substantial impact on material performance. For example, samples of NbO_2F and TaO_2F prepared via solution routes (rather than conventional solid-state routes) were found to have vacancies and hydroxide (OH^-) ions, which were introduced during preparation[140]. In the same study, it was shown that precise solid-state preparation of the materials produced samples with less vacancies or hydroxide contamination. The X-ray data of the phases prepared by the solid state route could be treated with a supercell model to describe the anion ordering motif.

Another example of a ReO_3-type oxyfluoride is VO_2F, which was applied as a cathode material[134]. For context, it is best to define the terminology, as well as provide reference points for battery comparison. Commercialized lithium ion batteries have specific capacities of between 100 and 200 mAh g^{-1} at a voltage of about 3.7 V, and will last between 600 and 3000 cycles[141]. The C-rate describes the charge and discharge rates of a battery, and the optimal C-rate depends on the application. A C-rate of 1 corresponds to a battery discharging completely in 1 h (a C-rate of 2 corresponds to a battery discharging twice as fast.) Typically, higher C-rates reduce achievable capacities for batteries because more stress is put onto the device. When VO_2F (theoretical capacity of 462 mAh g^{-1}) was applied as a cathode, it demonstrated a reversible capacity of 250 mAh g^{-1} at 2.2 V (one equivalent of Li, C/50 with graphene additive). However, if the material is cycled past 2.2 V (more than one equivalent of Li, C/50), it undergoes a conversion reaction, which reduces its cycling performance. This work was followed by a report where VO_2F prepared via ball-milling (as opposed to the high-temperature solid-state synthesis of the original report[142]) had a reversible cyclability of 208 mAh g^{-1} at 2.2 V, but at an improved cycle rate of C/20. If cycled to lower voltages, this VO_2F material undergoes an irreversible phase change, to what has been shown to be a disordered rock-salt phase[142–144]. This material was reported[144] to deliver 276 mAh g^{-1} (1.04 mol Li) and 206 mAh g^{-1} (0.8 mol Li) at C/20 in its first and second cycles, respectively, with 97.5% capacity maintenance after 100 cycles. If taken to the irreversible rock-salt phase, 406 mAh g^{-1} (1.54 mol Li, C/60) capacity was achieved, but with only 60% capacity retention after 50 cycles.

Hydroxides. The ReO_3-type hydroxides, commonly (and confusingly) referred to in the literature as hydroxide perovskites, $M(OH)_3$ or $MM'(OH)_6$, are a naturally occurring class of ReO_3-type materials well known to mineralogists[145], with some synthetic examples joining the ranks. Although there is still much to be understood about their fundamental crystal chemistry, members of this material class show promise as oxygen evolution reaction (OER) catalysts.

The single ReO_3-type hydroxides, $M(OH)_3$, include varieties where M^{III} = Al (REF.[146]), Ga REF.[147]), Fe (REFS[148,149]), Sc (REF.[150]), In (REFS[150,151]), Lu (REF.[152]) or Yb (REF.[153]). The gallium, indium and iron phases occur naturally, although all except for iron can be prepared synthetically. The most common preparations are metathesis reactions, usually between a MCl_3 species and NaOH (to form a gel), which is then washed and heated with more base to crystallize the compound. Early reports of the scandium[150], indium[150,151] and lutetium[152] compounds described their structures, including a neutron diffraction study to establish the locations of the hydrogen atoms[152]. In the case of $In(OH)_3$ (FIG. 5a), we draw attention to how the hydrogen bonding follows a four-ring (square) pattern; however, there are also 'zigzag' and 'crankshaft' hydrogen bonding patterns, which guide the structures of the hydroxide materials[145].

Pure $Yb(OH)_3$ has eluded synthetic efforts, although it is known to form solid solutions (up to 25% ytterbium) with both $Lu(OH)_3$ and $In(OH)_3$ (REF.[153]). As stated, $Fe(OH)_3{\cdot}nH_2O$ (bernalite) is a curious case[154]. There are no definitive reports of a laboratory-prepared ReO_3-type $Fe(OH)_3$, but there are reports of a 'Fe$(OH)_3$ powder', which is distinct from the $Fe(OH)_3$ gels that form in high-pH Fe^{3+} cation-containing solutions. This powder, we suspect, is the amorphous version of the ReO_3-type compound, with considerable disorder owing to water molecules inside the cavities. This $Fe(OH)_3$ powder has been studied with Mössbauer and magnetic susceptibility techniques to differentiate it from the gels, albeit without definitive structural characterization[148,149]. For the most part, these single-metal materials have fewer applications than the double hydroxides, although $In(OH)_3$ can be synthesized with nanomorphology and has been converted to the more industrially relevant In_2O_3 whilst maintaining its nanostructure[155].

There are numerous mineral examples of double ReO_3-type hydroxides, $MM'(OH)_6$, with a heavy predominance of stannates (the formal precursor is stannic acid, $Sn(OH)_4$). Some examples are $CaSn(OH)_6$ (burtite), $FeSn(OH)_6$ (natanite), $ZnSn(OH)_6$ (vismirnovite) and $MnSn(OH)_6$ (wickmanite)[145]. These stannate minerals crystallize in cubic space groups (except for $MnSn(OH)_6$, which is reported to be tetragonal) and exhibit cation ordering. There are also other minerals, such as $Fe^{3+}Sn^{4+}(OH)_5O$ (jeanbandyite), $NaSb^{5+}(OH)_6$ (mopungite) and $Fe^{2+}Ge^{4+}(OH)_6$ (stottite), that are not stannates. Synthetic varieties of double ReO_3 hydroxide compounds, such as $CuSn(OH)_6$ (REF.[156]), $CoSn(OH)_6$ (REF.[157]) and $SrSn(OH)_6$ (REF.[158]), are also known, with the latter example by Woodward and co-workers illustrating that the ionic sizes and electronegativities of the M-site cations are important characteristics for ReO_3-type structure formation. This concept was made evident by demonstrating that $LiSb^{5+}(OH)_6$ and $BaSn(OH)_6$ both crystallize in other structural motifs[158].

Magnetic studies of double ReO_3-type hydroxide materials have revealed that materials with strong charge ordering (for example, $MnSn(OH)_6$ and $CoSn(OH)_6$) are paramagnetic down to 2 K, but with $CoSn(OH)_6$ displaying uncompensated spin interactions near 28 K owing to the single-anion anisotropy of the octahedral Co^{II} atom[157]. $FeSn(OH)_6$ and $FeSn(OH)_5O$ (where the former forms the latter when left in air for a few hours) have also been examined[159], with $FeSn(OH)_6$ exhibiting paramagnetism down to 1.4 K and $FeSn(OH)_5O$ ordering antiferromagnetically at 4 K. Additionally, bulk Jahn–Teller-distorted $CuSn(OH)_6$ (REF.[156]) displays weak antiferromagnetic behaviour and a spin-Peierls transition in strong magnetic fields at about 78 K (REF.[160]).

Double ReO_3-type hydroxide materials have found recent relevance as both photocatalysts and OER catalysts. Their photocatalytic performance is linked to how, when exposed to ultraviolet light, they generate $OH^{\bullet-}$ radicals, which can degrade organic molecules[161]. The compounds $ZnSn(OH)_6$ (REF.[162]) and $CoSn(OH)_6$ (REF.[163]) have been of particular focus. The power of defect engineering to improve OER performance was demonstrated by the out-performance of an argon plasma-treated sample of $Co_{0.90}Fe_{0.10}Sn(OH)_6$ compared with a non-plasma-treated sample[164]. Owing to the weak Sn–OH bonds, argon plasma treatment selectively removes tin to expose more active iron and cobalt sites, while increasing the micropore size of the material. The treated sample required a much lower overpotential for catalysis (270 mV at 10 mA cm^{-2}, with a Tafel slope of 42.3 mV dec^{-1}) than the non-plasma-treated material (420 mV at 10 mA cm^{-2}, with a Tafel slope of 77.0 mV dec^{-1}). For context, the lower the Tafel slope[165], the more rapid the kinetics for OER (whilst holding reaction conditions constant). In another example, an electrochemical activation process was used to remove the Sn^{4+} cations from the SnFeNi hydroxide system[166]. The resulting SnFeNi hydroxide material performed comparably with the well-known OER material IrO_2. With the added benefit of being made from Earth-abundant metals, these tin-containing hydroxides are a promising direction for material research.

As indicated in the examples above, control over the vacancies and morphology of a double ReO_3-type hydroxide are essential to their use as functional materials. Such chemical control was exemplified by Nielson et al.[157], who demonstrated that if the hydrolysis of the Sn^{4+} ion can be kinetically controlled during the formation of $CoSn(OH)_6$ and $MnSn(OH)_6$ (by using a competing F^- anion), then defined charge ordering of the metals can be achieved. This control is significant because if charge ordering can be maximized, then materials like OER catalysts should have the maximum number of surface-active sites available after argon plasma treatment.

Lastly, the ordering of the metals affects the hydrogen-bonding tendencies in certain systems, which, as stated above, is a strong guide for the structure of the ReO_3-type hydroxides. In future work, it will be important to explore how greater synthetic control might encourage certain hydrogen-bonding arrangements (that is, different polymorphs). Mineralogists have highlighted some of the significant, more fundamental questions in this class of materials[145], with the overarching problem being that the crystallographic understanding (for example, space groups) of most ReO_3-type hydroxides is not definitive. This is an area where better synthetic control could elucidate why certain polymorphs are favoured in certain systems. Specifically, studies with variable temperature and pressure[167] may unravel the poorly understood phase transitions of these materials. Finally, with an average cavity diameter of 4.5 Å, small molecules could be intercalated into hydroxide materials; however, understanding how the hydroxide groups may play a role in guest-molecule intercalation is an open question.

Alloys. Skutterudite is a mineral that was named after the city of Skotterud, Norway, where it was first discovered in 1845. The naturally occurring version is a cobalt arsenide, $CoAs_3$, which also contains some nickel and iron on the cobalt site (FIG. 5b). The structure of the mineral form was first examined by X-ray diffraction in 1928 by Oftedal[168], who showed that it was cubic with space group $Im\bar{3}$. A more precise determination was carried

out by Mandel and Donohue in 1971 (REF.[169]). The structure is formed from a network of corner-sharing $CoAs_6$ octahedra, as in ReO_3; however, these octahedra are sufficiently tilted that the arsenic atoms form approximately planar As_4 units (FIG. 5b). For the As_4 unit to be square, the x and y values of the As coordinates must obey the so-called Oftedal relationship, $2(y + z) = 1$. However, in the determination by Mandel and Donohue, the values of x and y are such that the As_4 unit is rectangular with edges of 2.57 and 2.46 Å, respectively. There is a significant amount of As–As bonding in $CoAs_3$; hence, the system can be regarded as a Zintl phase[170]. The structure is analogous to that of $In(OH)_3$, where the hydrogen bonding creates a square pattern (FIG. 5a), and indeed the two systems adopt the same $Im\bar{3}$ space group. Several closely related families of naturally occurring and synthetic alloys adopt the skutterudite structure. This MX_3 family is known for M = Fe, Co, Ni, Ru, Rh, Ir or Os and X = As, Sb or P. However, we are not aware of any examples with M-site ordering, which is common for more ionic systems, as discussed previously.

The so-called 'filled skutterudites' are an exceptionally important extension of the skutterudite family. The first examples were reported by Jeitschko and Braun[171], and can be thought of as A-site deficient perovskites, A_xMX_3, with $x = 0.25$ (that is, their general composition is AM_4X_{12}). We have chosen to include them in this Review because they are closer in composition to ReO_3 than perovskite and because of their interesting electronic properties. Typical cases include systems such as LnM_4X_{12}, where Ln = rare earth, M = Fe, Ru or Os and X = P, As or Sb. Superconductivity below 4.08 and 7.20 K was reported for $LaFe_4P_{12}$ and $LaRu_4P_{12}$, respectively, in 1981 by Meisner[172], and magnetic ordering was found to occur at even lower temperatures when lanthanum was substituted by magnetic rare-earth elements, such as cerium, praseodymium and neodymium (superconductivity was not observed in the magnetic systems).

The initial discovery of superconductivity in $LaFe_4P_{12}$ and $LaRu_4P_{12}$ attracted the attention of the condensed-matter physics community and led to a large body of work on these materials. Beyond studies on superconductivity, the most exciting development was the establishment by Sales et al. in 1996 that some of the filled skutterudites were excellent thermoelectric materials with figures of merit (zT) in excess of 1.0 (REF.[173]). It was already recognized that conventional skutterudites had the possibility to be good thermoelectrics[174], and filled skutterudites offer the opportunity for enhancement of their thermoelectric performance. In particular, the rattling of the cations in the large A-site voids (FIG. 5c), along with the ease with which disorder can be introduced into these systems, contribute to their excellent performance. These factors reduce the lattice thermal conductivity by scattering phonons as discussed by Snyder and Toberer[175]. Subsequent developments in this area, including the use of filler cations with different charges, enabled the tuning of the carrier density, leading to systems with thermoelectric performance approaching that of state-of-the-art materials[176]. For example, $CoSb_3$ filled with various combinations of barium, lanthanum and ytterbium has zT values of up to 1.7 at 850 K (for example, $Ba_{0.08}La_{0.05}Yb_{0.04}Co_4Sb_{12}$)[177], which are close to the highest values reported to date for stable materials operating at these temperatures.

The bulk of the work on skutterudites for thermoelectric and other applications has focused on filled systems. However, an excellent figure of merit was reported for an unfilled system in which the thermal conductivity was minimized by controlling the nanostructure and microstructure of the material by means of careful annealing[178]. In this way, zT of 1.6 was obtained for a synthetic alloy of composition $Co_{23.4}Sb_{69.1}Si_{1.5}Te_{6.0}$, despite the absence of rattling cations in the A-site cavity. When the nanostructure and microstructure were not controlled by annealing, the thermal conductivity was approximately 4–5 times higher, leading to a 60% decrease in zT.

Cyanides. In view of the extensive literature on perovskite-related cyanides, such as Prussian blue, $Fe_4[Fe(CN)_6]_3{\cdot}xH_2O$ (REF.[179]), it is not surprising that similar ReO_3-type cyanides are known. These materials are generally referred to as Prussian blue analogues, although the literature does not differentiate between those that have cations on the A-sites (that is, perovskites) and those that do not (that is, ReO_3 types). Several cyanide-based examples with the ReO_3-type structure are known, including numerous bimetallic systems, such as $M^{II}Pt^{IV}(CN)_6$ (REF.[180]), $Ga^{III}Fe^{III}(CN)_6$ (REF.[181]) and $Fe_4[Ru(CN)_6]_3{\cdot}18H_2O$ (REF.[182]). The A-site cavities are larger than those of the simple oxides and fluorides, and, as a result, often contain solvent, typically water. Anhydrous materials, solvated systems and thiocyanates are the focus of this section.

The simplest cyanide-based compounds are those where M = Al (REF.[183]), Ga (REFS[184,185]) or In (REF.[186]). These materials are cubic, display varying degrees of cyanide disorder and are porous. For example, in the case of $In(CN)_3$, the compound incorporates krypton reversibly and hexane irreversibly[186]. In terms of single-metal cyanides, $Fe[Fe(CN)_6]$, normally described as $Fe(CN)_3$, is a particularly interesting case. It crystallizes in a doubled ReO_3-type structure with alternate Fe^{III} ions coordinated by six carbon atoms and six nitrogen atoms from the cyanide ions[187] (FIG. 6a). $Fe[Fe(CN)_6]$ is sometimes known as Berlin green because of its historical use as a pigment in paintings. The cation ordering, which gives rise to the doubling of the basic ReO_3 unit cell, is made possible by having the two iron sites in low-spin d^5 (FeC_6) and high-spin d^5 (FeN_6) states. The cavity in the as-synthesized material contains some water, which can be removed under vacuum; samples of the anhydrous material have been studied as a function of temperature by synchrotron X-ray diffraction[187]. $Fe[Fe(CN)_6]$ can be prepared in bulk or with microstructured morphology without the need for surfactants by using $K_3[Fe(CN)_6]$ and $Na_2S_2O_3$ as precursors[188]. Like many ReO_3-type structures, it exhibits pronounced NTE over a wide temperature range, in this instance from 100 to 450 K (REF.[179]). In a similar manner to the ReO_3-type oxides and fluorides, NTE is associated with transverse vibrations of the carbon and nitrogen atoms of the cyanides; these are especially strong for the nitrogen atoms owing to the long Fe–N bonds. In a variation on this theme, a

guest dependence of NTE was reported for $M^{II}Pt^{IV}(CN)_6$ (M = Zn, Cd) by Goodwin et al.[98]. The study showed that the transverse vibrations are dampened and NTE is suppressed by the inclusion of intercalated water (FIG. 6b). As a point of interest, this dampening of NTE via intercalation is also observed for a related (non-ReO_3-type) porous rare-earth cyanide compound[189], illustrating the similar structure–property relationships between this and the $M^{II}Pt^{IV}(CN)_6$ system.

The magnetic properties of a hydrated form of $Fe[Fe(CN)_6]$ have been studied by low-temperature neutron diffraction, Mössbauer spectroscopy and magnetic susceptibility methods, with the system having been found to undergo a paramagnetic–ferromagnetic phase transition on cooling to 17.4 K (REF.[190]). This observation is consistent with the weak ferromagnetic exchange coupling that is expected between low-spin d^5 Fe^{III} and high-spin d^5 Fe^{III} via the cyanide linker. There is also a long history of bimetallic Prussian blue analogues that have been studied for their magnetic properties[191], mainly in the context of molecular magnetism. This area is particularly fruitful because the alternation of two different octahedrally coordinated cations that are linked by cyanide groups can give rise to a wide range of antiferromagnetic, ferromagnetic and ferrimagnetic behaviour.

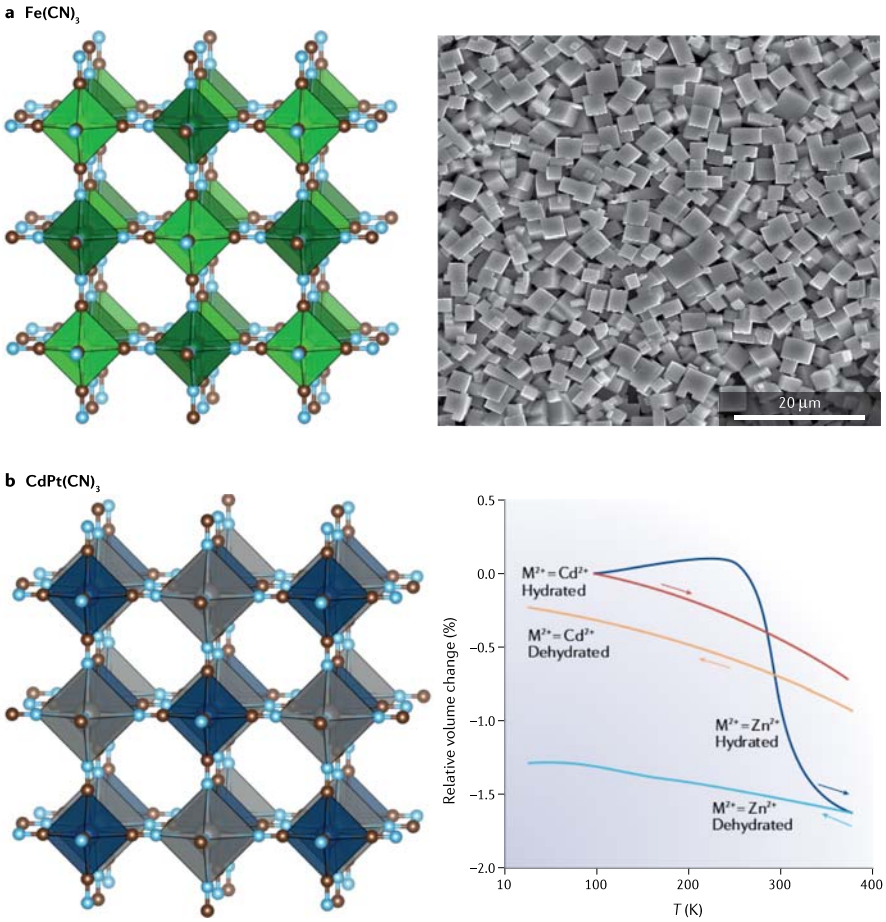

Fig. 6 | **Prussian blue analogue materials. a |** Structure of $Fe(CN)_3$ (left), with scanning electron microscope image of Berlin green microcubes (right). **b |** Structure of dehydrated $Cd^{II}Pt^{IV}(CN)_6$ (left), with graph showing the relative volume change as a function of temperature for $M^{II}Pt^{IV}(CN)_6$ (M = Zn, Cd) (right). The samples (as indicated by the arrows) were first heated (whereupon they dehydrated) and then cooled for the experiment. Intercalated water within the two compounds changes their negative thermal expansion behaviour by dampening the transverse vibrations of the –CN ligands. Atom legend: iron, light and dark green; carbon, brown; nitrogen, light blue; cadmium, grey; platinum, navy blue. Panel **a** (right) is adapted with permission from REF.[188], American Chemical Society. Panel **b** is adapted with permission from REF.[98], American Chemical Society.

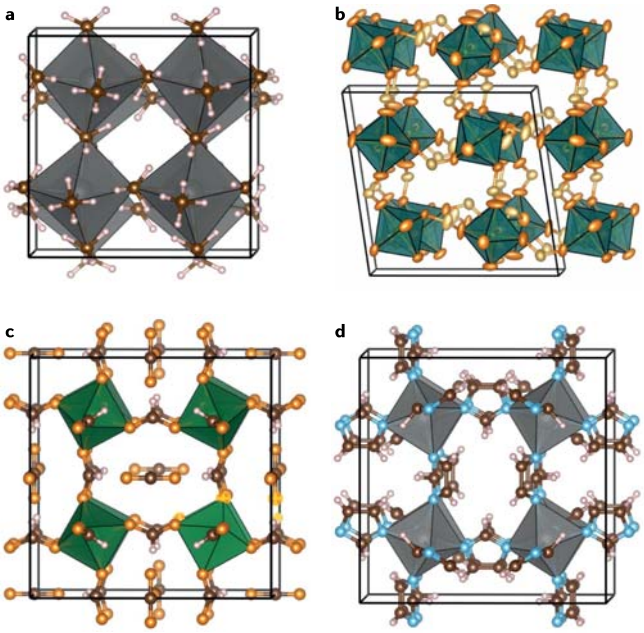

Fig. 7 | **ReO_3-type compounds with polyatomic linkers on the X-site. a** | Crystal structure of α-$Y(BH_4)_3$. Bonds are drawn between the Y and B atoms to emphasize the ReO_3-type structure, although these bonds are not present. In fact, the bonding between Y and H atoms guides the structure to be ReO_3-type[200]. Atom legend: yttrium, grey; boron, brown; hydrogen, white. **b** | Representative crystal structure with the ReO_3-type structure of α-$M(H_2PO_2)_3$, shown for M = Ga in the $P2_1/n$ space group (90% ellipsoids, H atoms removed for clarity)[211]. Atom legend: gallium, turquoise; oxygen, orange; phosphorous, beige. **c** | Crystal structure of $Fe(HCOO)_3$ with interstitial CO_2 (water removed for clarity)[220]. Atom legend: iron, green; oxygen, orange; carbon, brown; hydrogen, white. **d** | Crystal structure of $In(im)_3$. The imidazolate (im) anions arrange in an alternating pattern in $In(im)_3$ to accommodate their size. Atom legend: indium, grey; nitrogen, blue; carbon, brown; hydrogen, white.

Although research in this area has focused on systems with cations on the A-sites (which are therefore beyond the scope of this work), there are examples of magnetic cyanide-based materials that adopt the ReO_3-type structure. The most striking case is probably a phase with the approximate composition $VCr(CN)_6{\cdot}xH_2O$, which has a ferrimagnetic ordering temperature of 315 K owing to strong superexchange interactions between the V and Cr^{III} ions[192]. The system is more complex than it initially appears, however, because vanadium is present in both the V^{II} and V^{III} oxidation states, leading to various possible magnetic interactions. Other examples are the Co^{II}–Mn^{II}–Cr^{III} compounds $Co_xMn_{1-x}[Cr(CN)_6]_{2/3}{\cdot}zH_2O$ (REF.[193]), which, depending on the compound of choice within the family, can be tuned between ferromagnetic and antiferromagnetic coupling according to the relative humidity. The humidity-induced variations in these compounds are related to the coordination geometries of the cobalt ions, which in certain variants are undercoordinated owing to $[Cr(CN)_6]$ vacancies and can be coordinated by water. A counter example is the iron–ruthenium Prussian blue analogue $(Fe_4[Ru(CN)_6]_3{\cdot}18H_2O)$ (REF.[182]), which was examined in part for its potential magnetic behaviour but was found to display no ordering above 1.8 K. This material is nonetheless interesting because it demonstrates the effect of electron localization when compared with its Prussian blue parent and potassium-intercalated sibling $(K_{1.2}Ru_{3.6}[Ru(CN)_6]_3)$, as the iron–ruthenium compound has decreased electrical conductivity and blue-shifted optical intervalence charge-transfer transitions.

Many materials based on Prussian blue analogues have been explored for use in sodium-ion batteries[194]; however, work in this area has been hampered by low capacity and poor cyclability. In the case of $Fe[Fe(CN)_6]$, the use of nanoparticles overcame these drawbacks, giving rise to a device with good kinetics, capacity and lifetime[195,196] (we note that this strategy also worked for FeF_3, as discussed earlier). There has also been work on lithium[197] and potassium[198] batteries with $Fe[Fe(CN)_6]$.

Finally, we would like to mention a recent report on the first examples of thiocyanates with the ReO_3-type structure[199]. The thiocyanate systems have the general composition $M^{III}[Bi(SCN)_6]$ (with M = Fe, Cr, Sc), and there is strict alternation of Bi^{III} with the trivalent transition metal ions. This ordering is not surprising, given the expected local bonding preference between sulfur and Bi^{III}. These materials have band gaps in the visible or infrared regions, with the iron compound being as low as 1.20 eV, and are therefore strongly coloured and might be useful for applications that involve light harvesting. The A-site cavity is expected to be even larger than those in the cyanides described above; however, the porosity of thiocyanate systems is reduced owing to substantial monoclinic distortions of the hypothetical cubic structures. Nevertheless, the Cr^{III} compound exhibits reversible adsorption and desorption of water, forming a monohydrate. As in some of the other cyanides, the guest molecules influence thermal expansion; however, unlike cyanides, there is no NTE in these systems.

Borohydrides. M^{III} borohydrides, $M(BH_4)_3$, sometimes crystallize in the ReO_3-type structure depending on the synthetic route and the size of the metal ion. A well-studied example is $Y(BH_4)_3$ (FIG. 7a), a promising hydrogen-storage material that is attractive because it degrades to H_2 gas and solid YB_4 under 1–5 bar of partial hydrogen pressure (that is, a typical operating condition of a hydrogen-storage system)[200–202]. Unlike other M^{III} borohydrides, which have common by-products like elemental boron or diborane, YB_4 is more easily converted back to $Y(BH_4)_3$, enabling a charge–discharge cycle[203]. Crystallographically, $Y(BH)_4$ is reminiscent of the oxide ReO_3-type phases, because it has two ReO_3-type polymorphs, α and β, which are both generated during ball-milling and coexist at room temperature. However, the denser and more distorted α-$Y(BH_4)_3$ phase can be converted to the less dense and cubic β-$Y(BH_4)_3$ phase upon heating to 433–453 K, ultimately decomposing at temperatures above 463 K. However, in contrast with the oxides, both phases show monotonic positive thermal expansion.

A systematic study of the M^{III}–BH_4 reaction system with M = lanthanide[204] demonstrated the importance

of the ionic radius of the M metal in determining whether the ReO_3-type structure is formed. Using ball-milling with a $LiBH_4$ precursor, the larger lanthanides (that is, lanthanum, cerium, praseodymium and neodymium) formed only the cubic $LiM(BH_4)_3Cl$ structure, whereas those closer in size to yttrium (that is, antimony, gadolinium, terbium, dysprosium, erbium and ytterbium) all formed the α-$Y(BH_4)_3$ structure. The elements samarium, erbium and ytterbium are also stable in the β-$Y(BH_4)_3$ structure under certain conditions. Further experimentation yielded the distorted ReO_3-type $M(BH_4)_3$ (M = La, Ce) through the reaction of MCl_3 and $LiBH_4$ in toluene at room temperature, followed by extraction of $M(BH_4)_3$ using dimethyl sulfide $[S(CH_3)_2]$ to form a solvated phase. Subsequent loss of $S(CH_3)_2$ from the adduct yields the $M(BH_4)_3$ phase[205]. The $S(CH_3)_2$ templating strategy combined with halide-free reagents (that is, a rare-earth hydride and $S(CH_3)_2{\cdot}BH_3$) was then applied to generate new structures, including the cubic $Pa\bar{3}$ α-$Pr(BH_4)_3$ and α-$Nd(BH_4)_3$ structures[206], and α-$Ce(BH_4)_3$, β_2-$Pr(BH_4)_3$, α-$Lu(BH_4)_3$ and β-$Pr(BH_4)_3$ (REF.[206]). The structures of the $S(CH_3)_2$-adduct intermediates as layered phases, reminiscent of layered perovskites, were also identified[207]. Although the ReO_3 phases are not direct precursors, the related $Li(M(BH_4)_3)Cl$ phases may be used as fast lithium-ion conductors for solid-state battery electrolytes and gas storage[208], with some lithium borohydride phases having been tested in devices[209].

Hypophosphites. Until recently, the compound $V(H_2PO_2)_3$ was the only example of a hypophosphite-containing ReO_3-type compound[210]. From our recent work, $V(H_2PO_2)_3$ is now understood to be a member of a polymorphic family of ReO_3-type materials, $M(H_2PO_2)_3$, where M = Al, Ga or V (REF.[211]) (FIG. 7b). There are four polymorphs seen in this family (α, β, γ and δ), with each displaying different degrees of tilts and shifts of the M octahedra. Furthermore, the preference for each polymorph is determined by M, with each $M(H_2PO_2)_3$ forming at least two of the four polymorphs. The high-pressure (above 1 GPa) δ phase has been observed for $Ga(H_2PO_2)_3$, which prefers the less dense α phase at standard temperature and pressure. Synthetic control of each polymorph as a pure phase has yet to be achieved; however, to obtain at least one pure polymorph in each metal system, an acid-soluble oxide precursor should be used (such as γ-Al_2O_3 instead of corundum for the aluminium system). Interestingly, $Al(H_2PO_2)_3$ is an excellent bromine-free flame retardant in polymer blends[212]. As the structures of two polymorphs were only just reported for this system[211], the possibility that one polymorph may perform better as a flame retardant than the other has yet to be explored.

Summary for inorganic structures. Inorganic ReO_3-type materials are numerous and diverse. They range from single X-atom compounds, such as ReO_3 and ScF_3, to those with multiatom linkers, such as $Ga(CN)_3$ and $Al(H_2PO_2)_3$. In addition to compositional diversity, the properties are varied, although there are unifying themes between many compounds. These common themes include the sensitivity of magnetic and electronic properties to the M–X–M bond angles, and the ability to incorporate cations or neutral molecules in the A-site cavity. There are also many avenues for future research in this growing area. One example is to expand the families of double ReO_3-type materials; for example, currently only single-cation hypophosphites are known, but creating II–IV double ReO_3-type materials may introduce new properties into the family. In addition, the discovery of entirely new families of materials is possible. One example would be the azide (az) compounds $M(az)_3$, which may be explosive but could be promising as high-energy materials. Dicyanamides containing $N(CN)_2^-$ are also of interest; these materials are known to form as perovskites[213] but have yet be realized as an ReO_3-type material.

Metal–organic frameworks

We have seen in the previous section that there are several inorganic systems with the ReO_3-type structure in which the anionic linkers are polyatomic. Such compounds are an interesting variation on the perovskite structure type because the vacant A-site may create a space that is large enough to accommodate adsorbed solvent or small gas molecules. This behaviour is seen in the cyanides and the thiocyanates, although the cavity in the hypophosphites is too small for even monatomic neon[211]. As the cavities defined by the larger molecular X-sites may even be large enough to deliver permanent porosity, there is a similarity between such systems and MOFs. Therefore, it is not surprising to find that there are several examples of ReO_3-type materials in which the linker is an organic anion. Such materials can be properly regarded as MOFs. Examples of such systems include materials based on a wide variety of organic linkers, such as formates, azolates, guanidinates and other, more complex ligands. We shall discuss these materials below, including some examples in which the B-site cation is replaced by a polyatomic cation which preserves the ReO_3-type structure by acting as an octahedral node that is linked in 3D by suitable organic anions.

The nomenclature for these materials in the MOF literature is varied, and includes the use of the terms pcu, α-polonium and reo networks. For simplicity, we shall largely refer to them as ReO_3-type structures.

Formates. ABX_3 perovskite-type phases, where X = $(HCOO)^-$ (formate) and B (or M) = Mg, Mn, Fe, Co, Ni, Cu, or Zn, have been extensively studied, as they are easily prepared using solution synthesis and show a wide range of interesting ferroelectric, magnetic and multiferroic properties[214–216]. The classical Goldschmidt tolerance factor equation[217], which predicts the relative radii of cations and anions that are compatible with simple inorganic perovskite formation, has been extended to hybrid perovskites[218,219] and can be used to predict the sizes of the A cations that will stabilize the perovskite structure in systems such as $AM^{II}(HCOO)_3$. Because the cavity is quite substantial, large protonated amines, such as dimethylammonium, $(CH_3)_2NH_2^+$, are required. Although the tolerance factor equation is not

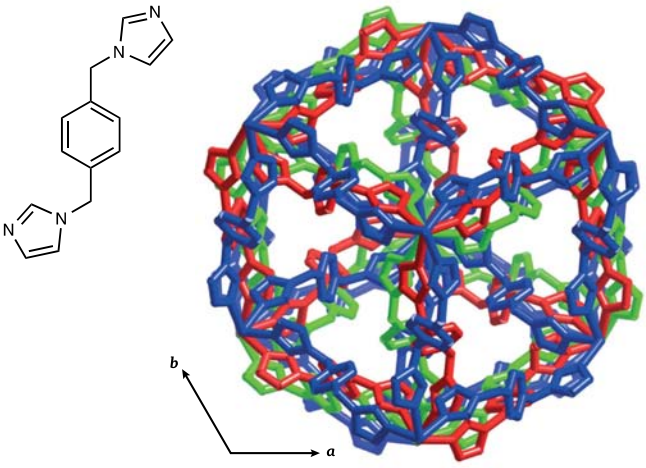

Fig. 8 | **Metal–organic framework with interpenetrating structure.** Triply interpenetrating metal–organic framework based on a bis-imidazole ligand. Adapted with permission from REF.[230], Royal Society of Chemistry.

strictly applicable to ReO_3-type structures, it is not surprising to find that ReO_3-type systems of composition $M^{III}(HCOO)_3$ have been reported, albeit only in the presence of neutral guest molecules that occupy the A-site cavities.

In 1965, it was reported that $V(HCOO)_3{\cdot}HCOOH$ crystallizes in the ReO_3-type structure[220], but a full structure determination for this compound has not been performed to date. However, the powder diffraction pattern[220] was indexed on a body-centred cubic structure that is consistent with M^{III} formates reported more recently[221]. In addition, some properties of $V(HCOO)_3{\cdot}HCOOH$, such as density, are close to the values reported for the $Fe(HCOO)_3{\cdot}$solvent phase (V^{3+} and Fe^{3+} having similar atomic weights and radii)[221]. The neutral formic acid molecule, HCOOH, is expected to occupy the A-site.

Recent work[221] on the $M^{III}(HCOO)_3$ systems (M = Al, Fe, Ga, In) confirmed that these phases, which can be readily formed by solvothermal or reflux methods, adopt an ReO_3-type structure with neutral A-site occupants assigned as combinations of H_2O, CO_2 and HCOOH (FIG. 7c). All of these phases crystallize in the cubic $Im\bar{3}$ space group with a = 11.4–12.2 Å. Unlike other carboxylate MOFs, the molecules occupying the A-sites in the $M^{III}(HCOO)_3$ systems could not be liberated while keeping the framework intact, suggesting that these molecules may have a structural role through strong hydrogen bonding or that the M–O bonds are insufficiently strong to stabilize the framework in the absence of guests. An alternative form of the $Fe(HCOO)_3{\cdot}$guest ReO_3-type phase was also reported[222], crystallizing in the trigonal $R\bar{3}c$ space group with a = 8.2 Å, c = 22.6 Å. It exhibits weak ferromagnetism below 50 K.

The formate ReO_3-type compounds could perhaps be regarded as the simplest MOF systems and can be made from inexpensive, Earth-abundant starting materials. Interestingly, they form preferentially in the presence of CO_2, and $Al(HCOO)_3{\cdot}xCO_2/yH_2O$ can be obtained by bubbling CO_2 through an aqueous solution containing $Al(OH)_3$ and formic acid[221]. The fully stoichiometric phase, $Al(HCOO)_3{\cdot}CO_2$, has yet to be achieved, but with a CO_2 loading of greater than 21 wt%, it is a possible material for CO_2 storage.

Nitrogen-containing organic linkers. In light of what has been reported for the formates, where the ReO_3-type MOFs contain metal–oxygen bonds, it is reasonable to expect that MOFs with the ReO_3-type structure might also form with nitrogen-containing organic linkers that are capable of metal–nitrogen bonding. This bonding has so far been realized for guanidinates, 1,2,4-triazolates and imidazolates, although there are other systems that might be feasible.

Only one guanidinate with the ReO_3-type structure is known to exist, $Yb(CN_3H_4)_3$ (REF.[223]). This phase was synthesized in liquid ammonia and crystallizes in the cubic $Pn\bar{3}$ space group with a = 13.5 Å. Braced by the extensive hydrogen bonding between guanidinate anions, it has a relatively low density (1.9 g cm^{-3}) and possible voids in its structure. Unlike many of the simple inorganic ReO_3-type systems, $Yb(CN_3H_4)_3$ shows positive thermal expansion rather than NTE. It is interesting to note that in perovskite and perovskite-related materials, guanidine can take the role of an anionic linker (guanidinate, as in $Yb(CN_3H_4)_3$) and an A-site cation (guanidinium, $C(NH_2)_3^+$, as in formate perovskites[224] and vacancy-ordered double perovskites[225]). Control of pH is important in determining which of these two roles it assumes, as a strongly alkaline environment is needed to stabilize the gaunidinate anion.

Although azolates are a well-known building block for MOFs (particularly zeolitic imidazolate frameworks, in which imidazolates are the linkers), they are primarily used in tetrahedral coordination with M^{II} cations. Nevertheless, there are a small number of ReO_3-type structures based on azolates. For example, $Yb(tz)_3$ (tz = 1,2,4-triazolate) was prepared from ytterbium metal and a melt of the azole, crystallizing in the cubic $Pm\bar{3}m$ space group with a = 6.8 Å (REF.[226]). $Yb(tz)_3$ is not strictly an ReO_3-type material, because some of the triazolate ligands coordinate in a bidentate manner; however, the overall architecture is ReO_3-like. This phase is well packed and shows no accessible porosity. $Ga(tz)_3$ was later reported[227], forming at the interface between the immiscible liquid Ga metal and liquid triazole. This phase crystallizes in the cubic $I23$ space group with a = 12.3 Å. Gas sorption testing showed that $Ga(tz)_3$ is also a dense framework with no accessible porosity. We are not aware of any ReO_3-type structure based on 1,2,3-triazolate linkers.

More recently, imidazole was successfully used to form $In(im)_3{\cdot}xG$ (G = guest) ReO_3-type phases via different pathways, including ionothermal, solvothermal and solventless syntheses[228]. Three phases were obtained — phases I, II and III — with structural parameters of $Im\bar{3}$, a = 13.0 Å; $R\bar{3}$, a = 18.9 Å, c = 10.5 Å; and $R\bar{3}$, a = 9.1 Å, c = 22.3 Å (FIG. 7d). Although gas sorption showed no accessible porosity, varying amounts of

unbound neutral molecules were trapped inside the framework cavities of phases I and II. Phase III was reported as a dense, guest-free structure. All structures were solved by powder X-ray diffraction, and the identities and quantities of neutral guest molecules in phases I and II were assigned by NMR spectroscopy to a range of molecules, including solvent and products of solvent decomposition[228]. The structures were distinguished by different octahedral tilting patterns. Phases I and II showed a reversible, discontinuous, hysteretic phase transition at ~363 K. The synthesis method affected the transition temperature, likely owing to the different guest molecules trapped within the framework. It seems unlikely that In^{III} is the only trivalent cation capable of forming ReO_3-type networks with imidazolate; thus, this is an interesting area for future exploration.

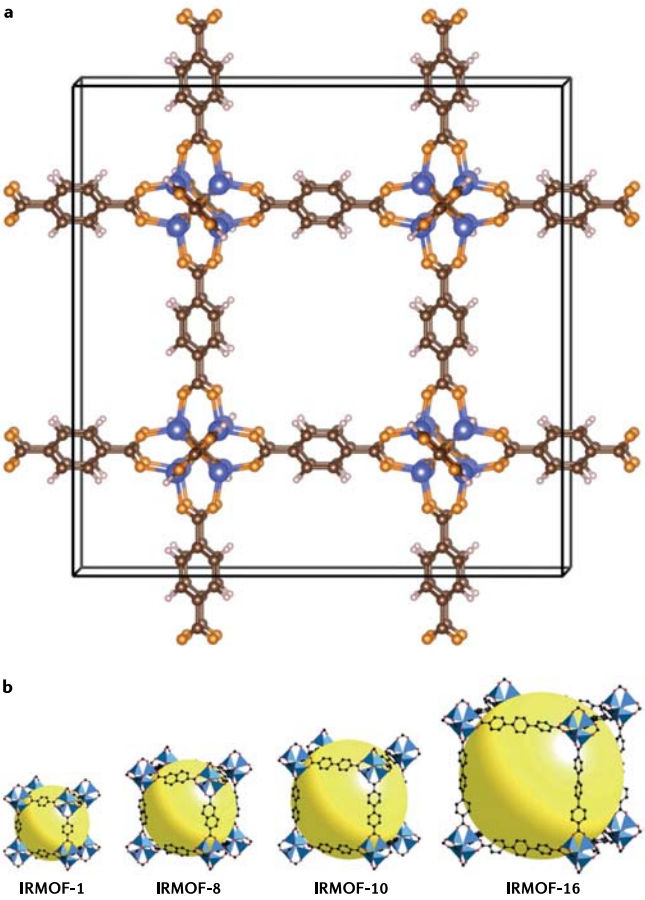

Fig. 9 | **MOFs with polyatomic B-site cations. a** | Structure of the metal–organic framework (MOF) MOF-5, with a Zn_4O unit on the octahedra B-site node and 1,4-bezenedicarboxylate anions on the X-site, of an ReO_3-type structure[16]. This structure type is referred to as pcu (primitive cubic) in the MOF community. Atom legend: zinc, light blue; oxygen, orange; carbon, brown; hydrogen, white. **b** | Isoreticular MOFs (IRMOFs), where IRMOF-1 = MOF-5. Atom legend: zinc, light blue; oxygen, red; carbon, black; yellow, void space. Panel **b** is adapted with permission from REF.[253], Royal Society of Chemistry.

Systems with complex linkers. There are several examples of positively-charged ReO_3-type MOFs with large organic linkers and charge-compensating anions in their A-site cavities[229], but these are more like perovskites than ReO_3 systems (albeit with inverse polarity). These structures are sometimes referred to in the MOF literature as having an α-polonium-type structure (α-Po being the only simple cubic metal structure), irrespective of their charged framework and the presence of anions in the A-site cavities. An important example is provided by the large, neutral bis-imidazole ligands (FIG. 8), which form ReO_3-type frameworks with Cd^{2+} nodes[230]. It is particularly interesting that the frameworks are triply interpenetrating, presumably to reduce the unoccupied space in the channels. Such behaviour is also seen in some MOF-5-related materials discussed below. The positive charges of the frameworks in these structures are balanced by nitrate or tetrafluoroborate anions, which sit in the small cavities created by the interpenetrating ReO_3 nets. One would imagine that neutral frameworks of this type could be obtained using a trivalent cation in combination with anionic ligands.

MOFs with polyatomic B-site cations. In this final section on MOFs with the ReO_3-type structure, we shall focus on a more complex group of materials in which the cations on the B-site are polyatomic clusters linked by organic ligands. The most iconic example is MOF-5, where tetrahedral $Zn_4O_6^+$ clusters are connected by 1,4-benzenedicarboxylate (1,4-bdc) anions to form a 3D network of composition $[Zn_4O](1,4\text{-bdc})_3$ (REF.[16]) (FIG. 9a). This important discovery from Yaghi's group led to the concept of reticular synthesis[231,232], whereby structures with even larger cavities could be obtained using longer linkers (FIG. 9b). By so doing, it is possible to tune the porosity of the MOF system for specific applications. This family of MOFs is, therefore, justifiably famous for being a model for the optimization of porous frameworks for applications in separation and catalytic processes[233]. As with many ReO_3-type structures, MOF-5 itself exhibits NTE[234]. We note that interpenetration is often found in structures containing longer linkers, which are used to synthesize some isoreticular MOFs, although steps can be taken to mitigate this outcome.

There can be endless variations on the MOF-5 theme if we allow for the possibility that the 1,4-benzenedicarboxylate linker might bear substituents on the benzene rings. Yaghi and co-workers reported examples including $-NH_2$, –Br, –Cl and $-NO_2$, and referred to such systems as multivariate MOFs on account of the range of compositional variations that are possible, such as combining eight distinct functionalities into a single phase[235,236]. The chemical variations are not solely of academic interest because it is possible to tune the adsorption behaviour of MOFs for particular applications. For example, by fine-tuning the composition of the MOF, the selectivity for CO_2 adsorption can be enhanced by up to 400% compared with CO adsorption[235]. Although we are not aware that this class of materials is being used

Table 1 | **Unknown ReO_3 analogues of known perovskite families or vice versa**

Perovskite family	ReO_3 analogue
(AmineH)PbX_3	BiX_3 (not reported)
$A^IB^{II}(OH)_3$ (not reported)	$M^{III}(OH)_3$
(AmineH)$M^{II}(N_3)_3$	$M^{III}(N_3)_3$ (not reported)
(AmineH)M^{II}(gua)$_3$ (not reported)	M^{III}(gua)$_3$
(AmineH)M^{II}(im)$_3$ (not reported)	M^{III}(im)$_3$
(AmineH)M^{II}(1,2,4-triazole)$_3$ (not reported)	M^{III}(1,2,4-triazole)$_3$
(AmineH)M^{II}(1,2,3-triazole)$_3$ (not reported)	M^{III}(1,2,3-triazole)$_3$ (not reported)
(AmineH)M^{II}(tetrazole)$_3$ (not reported)	M^{III}(tetrazole)$_3$ (not reported)
(AmineH)M^{II}(dicyanamide)$_3$	M^{III}(dicyanamide)$_3$ (not reported)

The unknown phases are indicated as not reported. In some cases, such as with 1,2,3-triazole, both are unknown but might be expected to form. gua, guanidinate; im, imidazolate.

commercially, the concepts described are being used in other areas of MOF research.

There are symmetry constraints on the types of compounds that can form an ReO_3-type network, because the building unit at the B-site node must be compatible with 6-fold connectivity[237]. This 6-fold connectivity is achieved in MOF-5 by using the two oxygen atoms from one end of the 1,4-benzenedicarboxylate carboxylate linkers to bond to two different zinc ions in the cluster. In spite of this constraint, there are many other examples of systems that adopt the ReO_3-type structure (which is often referred to as the pcu topology in the MOF literature, although this appellation is sometimes interpreted more loosely than we have done in this Review). Eye-catching examples include a system in which the nodes use $Cu_2(CO_2)_4$ paddlewheel clusters as vertices[238], and MFU-4 in which octahedral nodes based on $(Zn_5Cl_4)^{6+}$ are linked by linear bis-triazolate ligands[239]. To give a sense of the scope of this area, we note that Snurr and co-workers have explored the methane storage and delivery capacity of 122,835 hypothetical pcu frameworks[240] from the MOF database of Wilmer et al.[241]. Although the majority of these frameworks have not been synthesized, a small number of them are predicted to have exceptional properties.

Many other MOFs that are described in the literature as of pcu type are not included here because they do not preserve the cubic or pseudo-cubic architecture of the ReO_3-type structures. Typically, they have different linkages along different axes, such as the pillared–layered phases[242,243] and other structures based on paddlewheel nodes[244].

Summary for ReO_3-type MOFs. The study of MOFs with the ReO_3-type structure is less well developed than the inorganic area, but is a rapidly developing field full of exciting opportunities. We note, in particular, that the ability to tune the size of the A-site cavity by changing the length of the organic linker can be achieved in MOFs but is not practical in inorganic systems. Consequently, the MOF materials are far more versatile for adsorption applications. Similarly, the option of tuning the chemical environment of the A-site cavity by changing the substituents on the linker ligands means that it is possible to, for example, make a cavity more polar or more acidic than it would be with a chemically unmodified linker. This versatility is usually not possible with inorganic frameworks. However, the inorganic materials are usually more thermally stable, and they typically offer better mechanical stability than is found in MOF systems[245].

Concluding remarks

The chemical diversity of materials with the ReO_3-type structure is much greater than we had imagined when we began to think about this article in mid 2018. Furthermore, their properties and applications, both actual and potential, have also surpassed our expectations. The timeline shown in FIG. 2 highlights some of the important systems that have been developed over the last 80 years or more, from their initial discovery or structural characterization to the demonstration of their most striking properties. In addition to the remarkable range of their behaviour, we are struck by the long gaps between the initial discoveries of several of the materials and the establishment of their functionalities. In the case of ScF_3, for example, 70 years elapsed between the first structural characterization in 1939 (REF.[246]) and the recognition of its outstanding NTE behaviour in 2010. Several new ReO_3-type families have been reported in the past decade, including the borohydrides, hypophosphites, guanidinates and imidazolates, although the properties of these families are yet to be explored.

An exciting discovery in 2015 revealed the superconducting nature of hydrogen sulfide, H_2S. H_2S transforms to H_3S under high pressure, and this new phase is superconducting with a critical temperature of 203 K (REF.[247]). This property was predicted in 2014 (REF.[248]) and subsequent work in 2016 indicated that the superconducting H_3S phase adopts a doubly interpenetrating ReO_3 structure[249]. More recently, however, others have claimed that the superconducting phase is $(SH^-)(SH_3^+)$ and adopts the perovskite structure with (SH^-) on the A-site[250], and density functional theory calculations broadly support the idea of a disproportionation of H_2S (REF.[251]).

We noted at the beginning of the article that most of the ABX_3 perovskite families can form ReO_3 analogues, and vice versa, so it is appropriate at this point to revisit this issue and identify the structures where this has not yet been established. TABLE 1 presents several cases where the analogues are not known, or even where neither form is known but could exist. In some cases, such as the ReO_3 form of BiI_3, the compound prefers a layered structure, which is presumably stabilized by van der Waals interactions between the iodide ions. For the hypothetical $A^IB^{II}(OH)_3$, it might be that the protons that protrude into the A-site cavity render it unsuitable for hosting a metallic cation. However, there are several nitrogen-containing linkers that might lend themselves to the formation of new ReO_3-type or perovskite families, although we note that some of these may be high-energy materials, such as the azides and the tetrazoles. Future work in these areas is needed and has the potential to produce new ReO_3-type phases with interesting and unusual properties.

Published online 22 January 2020

1. Kojima, A., Teshima, K., Shirai, Y. & Miyasaka, T. Organometal halide perovskites as visible-light sensitizers for photovoltaic cells. *J. Am. Chem. Soc.* **131**, 6050–6051 (2009).
2. von Hippel, A. Ferroelectricity, domain structure, and phase transitions of barium titanate. *Rev. Mod. Phys.* **22**, 221–237 (1950).
3. Callaghan, A., Moeller, C. W. & Ward, R. Magnetic interactions in ternary ruthenium oxides. *Inorg. Chem.* **5**, 1572–1576 (1966).
4. Wu, M. K. et al. Superconductivity at 93 K in a new mixed-phase Y–Ba–Cu–O compound system at ambient pressure. *Phys. Rev. Lett.* **58**, 908–910 (1987).
5. von Helmolt, R., Wecker, J., Holzapfel, B., Schultz, L. & Samwer, K. Giant negative magnetoresistance in perovskite-like $La_{2/3}Ba_{1/3}MnO_z$ ferromagnetic films. *Phys. Rev. Lett.* **71**, 2331–2333 (1993).
6. Moreira dos Santos, A. et al. Evidence for the likely occurrence of magnetoferroelectricity in the simple perovskite, $BiMnO_3$. *Solid State Commun.* **122**, 49–52 (2002).
7. Cheetham, A. K. et al. Multiferroic behavior associated with an order–disorder hydrogen bonding transition in metal-organic frameworks (MOFs) with the perovskite ABX_3 architecture. *J. Am. Chem. Soc.* **131**, 13625–13627 (2009).
8. Ye, H.-Y. et al. Metal-free three-dimensional perovskite ferroelectrics. *Science* **361**, 151–155 (2018).
9. Li, W. et al. Chemically diverse and multifunctional hybrid organic–inorganic perovskites. *Nat. Rev. Mater.* **2**, 16099 (2017).
10. Woodward, P. M. Octahedral tilting in perovskites. II. Structure stabilizing forces. *Acta Crystallogr. B* **53**, 44–66 (1997).
11. Glazer, A. M. The classification of tilted octahedra in perovskites. *Acta Crystallogr. B* **28**, 3384–3392 (1972).
12. Woodward, P. M. Octahedral tilting in perovskites. I. Geometrical considerations. *Acta Crystallogr. B* **53**, 32–43 (1997).
13. Howard, C. J. & Stokes, H. T. Group-theoretical analysis of octahedral tilting in perovskites. *Acta Crystallogr. B* **54**, 782–789 (1998).
14. Duyker, S. G., Hill, J. A., Howard, C. J. & Goodwin, A. L. Guest-activated forbidden tilts in a molecular perovskite analogue. *J. Am. Chem. Soc.* **138**, 11121–11123 (2016).
15. Boström, H. L. B., Hill, J. A. & Goodwin, A. L. Columnar shifts as symmetry-breaking degrees of freedom in molecular perovskites. *Phys. Chem. Chem. Phys.* **18**, 31881–31894 (2016).
16. Li, H., Eddaoudi, M., O'Keeffe, M. & Yaghi, O. M. Design and synthesis of an exceptionally stable and highly porous metal–organic framework. *Nature* **402**, 276–279 (1999).
17. Zheng, H. et al. Nanostructured tungsten oxide—properties, synthesis, and applications. *Adv. Funct. Mater.* **21**, 2175–2196 (2011).
18. Ferretti, A., Rogers, D. B. & Goodenough, J. B. The relation of the electrical conductivity in single crystals of rhenium trioxide to the conductivities of Sr_2MgReO_6 and Na_xWO_3. *J. Phys. Chem. Solids* **26**, 2007–2011 (1965).
19. Mattheiss, L. F. Band structure and Fermi surface of ReO_3. *Phys. Rev.* **181**, 987–1000 (1969).
20. Tanisaki, S. Crystal structure of monoclinic tungsten trioxide at room temperature. *J. Phys. Soc. Jpn* **15**, 573–581 (1960).
21. Honig, J. M., Dimmock, J. O. & Kleiner, W. H. ReO_3 band structure in the tight-binding approximation. *J. Chem. Phys.* **50**, 5232–5242 (1969).
22. Sleight, A. & Gillson, J. Preparation and properties of alkali rhenium bronzes and a WO_3–ReO_3 solid solution. *Solid State Commun.* **4**, 601–602 (1966).
23. Chatterji, T., Hansen, T. C., Brunelli, M. & Henry, P. F. Negative thermal expansion of ReO_3 in the extended temperature range. *Appl. Phys. Lett.* **94**, 241902 (2009).
24. Purans, J. et al. X-ray absorption spectroscopy study of local dynamics and thermal expansion in ReO_3. *Phys. Rev. B* **92**, 014302 (2015).
25. Takenaka, K. Negative thermal expansion materials: technological key for control of thermal expansion. *Sci. Technol. Adv. Mater.* **13**, 013001 (2012).
26. Rodriguez, E. E. et al. The role of static disorder in negative thermal expansion in ReO_3. *J. Appl. Phys.* **105**, 114901 (2009).
27. Lind, C. Two decades of negative thermal expansion research: where do we stand? *Materials* **5**, 1125–1154 (2012).
28. Corà, F., Stachiotti, M. G., Catlow, C. R. A. & Rodriguez, C. O. Transition metal oxide chemistry: electronic structure study of WO_3, ReO_3, and $NaWO_3$. *J. Chem. Phys. B* **101**, 3945–3952 (1997).
29. Bozin, E. S., Chatterji, T. & Billinge, S. J. L. Local structure of ReO_3 at ambient pressure from neutron total-scattering study. *Phys. Rev. B* **86**, 3–6 (2012).
30. Jorgensen, J.-E., Jorgensen, J. D., Batlogg, B., Remeika, J. P. & Axe, J. D. Order parameter and critical exponent for the pressure-induced phase transitions in ReO_3. *Phys. Rev. B* **33**, 4793–4798 (1986).
31. Schirber, J. E. & Morosin, B. "Compressibility collapse" transition in ReO_3. *Phys. Rev. Lett.* **42**, 1485–1487 (1979).
32. Biswas, K. et al. Pressure-induced phase transitions in nanocrystalline ReO_3. *J. Phys. Condens. Matter.* **19**, 436214 (2007).
33. Muthu, D. V. S. et al. Pressure-induced structural phase transitions and phonon anomalies in ReO_3: Raman and first-principles study. *Phys. Rev. B* **91**, 224308 (2015).
34. Cava, R., Santoro, A., Murphy, D., Zahurak, S. & Roth, R. The structures of lithium-inserted metal oxides: $LiReO_3$ and Li_2ReO_3. *J. Solid State Chem.* **42**, 251–262 (1982).
35. Cava, R., Santoro, A., Murphy, D., Zahurak, S. & Roth, R. The structures of the lithium inserted metal oxides $Li_{0.2}ReO_3$ and $Li_{0.36}WO_3$. *J. Solid State Chem.* **50**, 121–128 (1983).
36. Bashian, N. H. et al. Correlated polyhedral rotations in the absence of polarons during electrochemical insertion of lithium in ReO_3. *ACS Energy Lett.* **3**, 2513–2519 (2018).
37. Santato, C., Odziemkowski, M., Ulmann, M. & Augustynski, J. Crystallographically oriented mesoporous WO_3 films: synthesis, characterization, and applications. *J. Am. Chem. Soc.* **123**, 10639–10649 (2001).
38. Cronin, J., Tarico, D., Tonazzi, J., Agrawal, A. & Kennedy, S. Microstructure and properties of sol–gel deposited WO_3 coatings for large area electrochromic windows. *Sol. Energy Mater. Sol. Cell* **29**, 371–386 (1993).
39. Sun, M., Xu, N., Cao, Y. W., Yao, J. N. & Wang, E. G. Nanocrystalline tungsten oxide thin film: preparation, microstructure, and photochromic behavior. *J. Mater. Sci.* **15**, 927–933 (2000).
40. Lee, S.-H. et al. Crystalline WO_3 nanoparticles for highly improved electrochromic applications. *Adv. Mater.* **18**, 763–766 (2006).
41. Baeck, S.-H., Choi, K.-S., Jaramillo, T., Stucky, G. & McFarland, E. Enhancement of photocatalytic and electrochromic properties of electrochemically fabricated mesoporous WO_3 thin films. *Adv. Mater.* **15**, 1269–1273 (2003).
42. Aird, A. & Salje, E. K. H. Sheet superconductivity in twin walls: experimental evidence of. *J. Phys. Condens. Matter.* **10**, L377–L380 (1998).
43. Wang, L., Teleki, A., Pratsinis, S. E. & Gouma, P. I. Ferroelectric WO_3 nanoparticles for acetone selective detection. *Chem. Mater.* **20**, 4794–4796 (2008).
44. Antonik, M. et al. Microstructural effects in WO_3 gas-sensing films. *Thin Solid Films* **256**, 247–252 (1995).
45. Galatsis, K., Li, Y., Wlodarski, W. & Kalantar-zadeh, K. Sol–gel prepared MoO_3–WO_3 thin-films for O_2 gas sensing. *Sens. Actuat. B Chem.* **77**, 478–483 (2001).
46. Li, X.-L., Lou, T.-J., Sun, X.-M. & Li, Y.-D. Highly sensitive WO_3 hollow-sphere gas sensors. *Inorg. Chem.* **43**, 5442–5449 (2004).
47. Ponzoni, A., Comini, E., Ferroni, M. & Sberveglieri, G. Nanostructured WO_3 deposited by modified thermal evaporation for gas-sensing applications. *Thin Solid Films* **490**, 81–85 (2005).
48. Ma, M. et al. Dual oxygen and tungsten vacancies on a WO_3 photoanode for enhanced water oxidation. *Angew. Chem. Int. Ed.* **55**, 11819–11823 (2016).
49. Zhang, J., Liu, Z. & Liu, Z. Novel WO_3/Sb_2S_3 heterojunction photocatalyst based on WO_3 of different morphologies for enhanced efficiency in photoelectrochemical water splitting. *ACS Appl. Mater. Interfaces* **8**, 9684–9691 (2016).
50. Li, W. et al. WO_3 nanoflakes for enhanced photoelectrochemical conversion. *ACS Nano* **8**, 11770–11777 (2014).
51. Hou, Y., Zuo, F., Dagg, A. P., Liu, J. & Feng, P. Branched WO_3 nanosheet array with layered C_3N_4 heterojunctions and CoO_x nanoparticles as a flexible photoanode for efficient photoelectrochemical water oxidation. *Adv. Mater.* **26**, 5043–5049 (2014).
52. Su, J., Feng, X., Sloppy, J. D., Guo, L. & Grimes, C. A. Vertically aligned WO_3 nanowire arrays grown directly on transparent conducting oxide coated glass: synthesis and photoelectrochemical properties. *Nano Lett.* **11**, 203–208 (2011).
53. Li, N. et al. Aqueous synthesis and visible-light photochromism of metastable h-WO_3 hierarchical nanostructures. *Eur. J. Inorg. Chem.* **2015**, 2804–2812 (2015).
54. Chen, Z. et al. Hierarchical nanostructured WO_3 with biomimetic proton channels and mixed ionic–electronic conductivity for electrochemical energy storage. *Nano Lett.* **15**, 6802–6808 (2015).
55. Yoon, S. et al. Development of a high-performance anode for lithium ion batteries using novel ordered mesoporous tungsten oxide materials with high electrical conductivity. *Phys. Chem. Chem. Phys.* **13**, 11060 (2011).
56. Girish Kumar, S. & Koteswara Rao, K. Tungsten-based nanomaterials (WO_3 & Bi_2WO_6): modifications related to charge carrier transfer mechanisms and photocatalytic applications. *Appl. Surf. Sci.* **355**, 939–958 (2015).
57. Kida, T. et al. WO_3 nanolamella gas sensor: porosity control using SnO_2 nanoparticles for enhanced NO_2 sensing. *Langmuir* **30**, 2571–2579 (2014).
58. Amano, F., Ishinaga, E. & Yamakata, A. Effect of particle size on the photocatalytic activity of WO_3 particles for water oxidation. *J. Phys. Chem. C* **117**, 22584–22590 (2013).
59. Chen, D. & Ye, J. Hierarchical WO_3 hollow shells: dendrite, sphere, dumbbell, and their photocatalytic properties. *Adv. Funct. Mater.* **18**, 1922–1928 (2008).
60. Wang, H., Dong, X., Peng, S., Dong, L. & Wang, Y. Improvement of thermoelectric properties of WO_3 ceramics by ZnO addition. *J. Alloy. Compd* **527**, 204–209 (2012).
61. Kieslich, G. et al. Using crystallographic shear to reduce lattice thermal conductivity: high temperature thermoelectric characterization of the spark plasma sintered Magnéli phases $WO_{2.90}$ and $WO_{2.722}$. *Phys. Chem. Chem. Phys.* **15**, 15399 (2013).
62. Kim, S.-J. et al. Mesoporous WO_3 nanofibers with protein-templated nanoscale catalysts for detection of trace biomarkers in exhaled breath. *ACS Nano* **10**, 5891–5899 (2016).
63. Shendage, S. et al. Sensitive and selective NO_2 gas sensor based on WO_3 nanoplates. *Sens. Actuators B* **240**, 426–433 (2017).
64. Rao, P. M. et al. Simultaneously efficient light absorption and charge separation in $WO_3/BiVO_4$ core/shell nanowire photoanode for photoelectrochemical water oxidation. *Nano Lett.* **14**, 1099–1105 (2014).
65. Tordjman, M., Weinfeld, K. & Kalish, R. Boosting surface charge-transfer doping efficiency and robustness of diamond with WO_3 and ReO_3. *Appl. Phys. Lett.* **111**, 111601 (2017).
66. Juza, R. & Hahn, H. Über die Kristallstrukturen von Cu_3N, GaN und InN Metallamide und Metallnitride. *Z. Anorg. Allg. Chem.* **239**, 282–287 (1938).
67. Paniconi, G. et al. Structural chemistry of Cu_3N powders obtained by ammonolysis reactions. *Solid State Sci.* **9**, 907–913 (2007).
68. Zhao, J., You, S., Yang, L. & Jin, C. Structural phase transition of Cu_3N under high pressure. *Solid State Commun.* **150**, 1521–1524 (2010).
69. Birkett, M. et al. Atypically small temperature-dependence of the direct band gap in the metastable semiconductor copper nitride Cu_3N. *Phys. Rev. B* **95**, 115201 (2017).
70. Terada, S., Tanaka, H. & Kubota, K. Heteroepitaxial growth of Cu_3N thin films. *J. Cryst. Growth* **94**, 567–568 (1989).
71. Asano, M., Umeda, K. & Tasaki, A. Cu_3N thin film for a new light recording media. *Jpn J. Appl. Phys.* **29**, 1985–1986 (1990).
72. Juza, R. & Hahn, H. Kupfernitrid metallamide und metallnitride. VII. *Z. Anorg. Allg. Chem.* **241**, 172–178 (1939).
73. Zakutayev, A. et al. Defect tolerant semiconductors for solar energy conversion. *J. Phys. Chem. Lett.* **5**, 1117–1125 (2014).
74. Kim, Y., Wieder, B. J., Kane, C. L. & Rappe, A. M. Dirac line nodes in inversion-symmetric crystals. *Phys. Rev. Lett.* **115**, 036806 (2015).
75. Pereira, N., Dupont, L., Tarascon, J. M., Klein, L. C. & Amatucci, G. G. Electrochemistry of Cu_3N with lithium. *J. Electrochem. Soc.* **150**, A1273 (2003).
76. Wu, H. & Chen, W. Copper nitride nanocubes: size-controlled synthesis and application as cathode catalyst in alkaline fuel cells. *J. Am. Chem. Soc.* **133**, 15236–15239 (2011).
77. Fischer, D. & Jansen, M. Synthesis and structure of Na_3N. *Angew. Chem. Int. Ed.* **41**, 1755–1756 (2002).

78. Vajenine, G. V. Plasma-assisted synthesis and properties of Na_3N. *Inorg. Chem.* **46**, 5146–5148 (2007).
79. Vajenine, G. V., Hoch, C., Dinnebier, R. E., Senyshyn, A. & Niewa, R. A temperature-dependent structural study of anti-ReO_3-type Na_3N: to distort or not to distort? *Z. Anorg. Allg. Chem.* **636**, 94–99 (2010).
80. Kim, D. et al. Type-II Dirac line node in strained Na_3N. *Phys. Rev. Mater.* **2**, 104203 (2018).
81. Zintl, E. & Brauer, G. Konstitution des Lithiumnitrids. *Z. Elektrochem.* **41**, 102–107 (1935).
82. Fischer, D., Cancarevic, Z., Schön, J. C. & Jansen, M. Zur synthese und struktur von K_3N. *Z Anorg. Allg. Chem.* **630**, 156–160 (2004).
83. Greve, B. K. et al. Pronounced negative thermal expansion from a simple structure: cubic ScF_3. *J. Am. Chem. Soc.* **132**, 15496–15498 (2010).
84. Groult, H. et al. Nano-CoF_3 prepared by direct fluorination with F_2 gas: application as electrode material in Li-ion battery. *J. Fluor. Chem.* **196**, 117–127 (2017).
85. Chaudhuri, S., Chupas, P. J., Wilson, M., Madden, P. & Grey, C. P. Study of the nature and mechanism of the rhombohedral-to-cubic phase transition in α-AlF_3 with molecular dynamics simulations. *J. Phys. Chem. B* **108**, 3437–3445 (2004).
86. Hepworth, M. A., Jack, K. H., Peacock, R. D. & Westland, G. J. The crystal structures of the trifluorides of iron, cobalt, ruthenium, rhodium, palladium and iridium. *Acta Crystallogr.* **10**, 63–69 (2002).
87. Daniel, P., Bulou, A., Leblanc, M., Rousseau, M. & Nouet, J. Structural and vibrational study of VF_3. *Mater. Res. Bull.* **25**, 413–420 (1990).
88. Siegel, S. The structure of TiF_3. *Acta Crystallogr.* **9**, 684–684 (1956).
89. Shannon, R. D. T. & Prewitt, C. T. Effective ionic radii in oxides and fluorides. *Acta Crystallogr. B* **25**, 925–946 (1969).
90. Shannon, R. D. Revised effective ionic radii and systematic studies of interatomic distances in halides and chalcogenides. *Acta Crystallogr. A* **32**, 751–767 (1976).
91. Hu, L. et al. New insights into the negative thermal expansion: direct experimental evidence for the "guitar-string" effect in cubic ScF_3. *J. Am. Chem. Soc.* **138**, 8320–8323 (2016).
92. Piskunov, S. et al. Interpretation of unexpected behavior of infrared absorption spectra of ReO_3 beyond the quasiharmonic approximation. *Phys. Rev. B* **93**, 214101 (2016).
93. Bhandia, R., Siegrist, T., Besara, T. & Schmiedeshoff, G. M. Grüneisen divergence near the structural quantum phase transition in ScF_3. *Philos. Mag.* **99**, 631–643 (2019).
94. Yang, C. et al. Size effects on negative thermal expansion in cubic ScF_3. *Appl. Phys. Lett.* **109**, 023110 (2016).
95. Hu, L. et al. Localized symmetry breaking for tuning thermal expansion in ScF_3 nanoscale frameworks. *J. Am. Chem. Soc.* **140**, 4477–4480 (2018).
96. Wang, T. et al. Tunable thermal expansion and magnetism in Zr-doped ScF_3. *Appl. Phys. Lett.* **109**, 181901 (2016).
97. Chen, J. et al. Tunable thermal expansion in framework materials through redox intercalation. *Nat. Commun.* **8**, 14441 (2017).
98. Goodwin, A. L., Chapman, K. W. & Kepert, C. J. Guest-dependent negative thermal expansion in nanoporous Prussian blue analogues $M^{II}Pt^{IV}(CN)_6 \cdot xH_2O$ ($0 \leq x \leq 2$; M = Zn, Cd). *J. Am. Chem. Soc.* **127**, 17980–17981 (2005).
99. Duan, N., Kameswari, U. & Sleight, A. W. Further contraction of ZrW_2O_8. *J. Am. Chem. Soc.* **121**, 10432–10433 (2002).
100. Phillips, A. E., Goodwin, A. L., Halder, G. J., Southon, P. D. & Kepert, C. J. Nanoporosity and exceptional negative thermal expansion in single-network cadmium cyanide. *Angew. Chem. Inter. Ed.* **47**, 1396–1399 (2008).
101. Phillips, A. E., Halder, G. J., Chapman, K. W., Goodwin, A. L. & Kepert, C. J. Zero thermal expansion in a flexible, stable framework: tetramethylammonium copper(I) zinc(II) cyanide. *J. Am. Chem. Soc.* **132**, 10–11 (2010).
102. Carey, T., Tang, C. C., Hriljac, J. A. & Anderson, P. A. Chemical control of thermal expansion in cation-exchanged zeolite A. *Chem. Mater.* **26**, 1561–1566 (2014).
103. Arai, H., Okada, S., Sakurai, Y. & Yamaki, J. I. Cathode performance and voltage estimation of metal trihalides. *J. Power Sources* **68**, 716–719 (1997).
104. Nishijima, M. et al. Cathode properties of metal trifluorides in Li and Na secondary batteries. *J. Power Sources* **190**, 558–562 (2009).
105. Zhou, M., Zhao, L., Doi, T., Okada, S. & Yamaki, J. I. Thermal stability of FeF_3 cathode for Li-ion batteries. *J. Power Sources* **195**, 4952–4956 (2010).
106. Takami, T. et al. Role of the particle size of Fe nanoparticles in the capacity of FeF_3 batteries. *AIP Adv.* **9**, 045301 (2019).
107. Yang, Z. et al. Atomistic insights into FeF_3 nanosheet: an ultrahigh-rate and long-life cathode material for Li-ion batteries. *ACS Appl. Mater. Interfaces* **10**, 3142–3151 (2018).
108. Jiang, J., Li, L., Xu, M., Zhu, J. & Li, C. M. FeF_3 thin nickel ammine nitrate matrix: smart configurations and applications as superior cathodes for Li-ion batteries. *ACS Appl. Mater. Interfaces* **8**, 16240–16247 (2016).
109. Kim, T. et al. A cathode material for lithium-ion batteries based on graphitized carbon-wrapped FeF_3 nanoparticles prepared by facile polymerization. *J. Mater. Chem.* **4**, 14857–14864 (2016).
110. Li, C., Gu, L., Tsukimoto, S., van Aken, P. A. & Maier, J. Low-temperature ionic-liquid-based synthesis of nanostructured iron-based fluoride cathodes for lithium batteries. *Adv. Mater.* **22**, 3650–3654 (2010).
111. Yang, Z., Pei, Y., Wang, X., Liu, L. & Su, X. First principles study on the structural, magnetic and electronic properties of Co-doped FeF_3. *Comput. Theor. Chem.* **980**, 44–48 (2012).
112. Liu, L. et al. Excellent cycle performance of Co-doped FeF_3/C nanocomposite cathode material for lithium-ion batteries. *J. Mater. Chem.* **22**, 17539 (2012).
113. Liu, L. et al. A comparison among $FeF_3 \cdot 3H_2O$, $FeF_3 \cdot 0.33H_2O$ and FeF_3 cathode materials for lithium ion batteries: structural, electrochemical, and mechanism studies. *J. Power Sources* **238**, 501–515 (2013).
114. Kitajou, A. et al. Novel synthesis and electrochemical properties of perovskite-type $NaFeF_3$ for sodium-ion battery. *J. Power Sources* **198**, 389–392 (2012).
115. Ruchaud, N., Mirambet, C., Fournes, L., Grannec, J. & Soubeyroux, J. L. Determination of the cationic arrangement in Sn_2F_6 from neutron powder diffraction. *Z. Anorg. Allg. Chem.* **590**, 173–180 (1990).
116. Köhl, P., Reinen, D., Decher, G. & Wanklyn, B. Strukturelle Modifikationen von $FeZrF_6$. *Z. Kristallogr. Cryst. Mater.* **153**, 211–220 (1980).
117. Mayer, H., Reinen, D. & Heger, G. Struktur und Bindung in Übergangsmetall-fluoriden $M^{II}Me^{IV}F_6$. *J. Solid. State Chem.* **50**, 213–224 (1983).
118. Bachmann, B. & Müller, B. G. Zur synthese und kristallstruktur von $LiPdAlF_6$ und $PdZrF_6$. *Z. Anorg. Allg. Chem.* **619**, 189–192 (1993).
119. Rodriguez, V. & Couzi, M. Structural phase transition in the ordered fluorides $M^{II}ZrF_6$ (M^{II} = Co, Zn). III. Landau theory. *J. Phys. Condens. Matter* **2**, 7395–7406 (1990).
120. Gerasimenko, A. V., Gaivoronskaya, K. A., Slobodyuk, A. B. & Didenko, N. A. Magnesium hexafluoridozirconates $MgZrF_6 \cdot 5H_2O$, $MgZrF_6 \cdot 2H_2O$, and $MgZrF_6$: structures, phase transitions, and internal mobility of water molecules. *Z. Anorg. Allg. Chem.* **643**, 1785–1792 (2017).
121. Friebel, C., Pebler, J., Steffens, F., Weber, M. & Reinen, D. Phase transitions in $CuZrF_6$ and $CrZrF_6$: a Mössbauer and EPR study of local and cooperative Jahn–Teller distortions. *J. Solid State Chem.* **46**, 253–264 (1983).
122. Schmidt, R., Kraus, M. & Müller, B. G. Neue fluorozirconate und -hafnate mit V^{2+} und Ti^{2+}. *Z. Anorg. Allg. Chem.* **627**, 2344–2350 (2001).
123. Le Mercier, T., Chassaing, J., Bizot, D. & Quarton, M. Structural, spectroscopic and magnetic studies of $V^{II}M^{IV}F_6$ compounds with M^{IV} = Zr, Nb. *Mater. Res. Bull.* **27**, 259–267 (1992).
124. Hester, B. R., dos Santos, A. M., Molaison, J. J., Hancock, J. C. & Wilkinson, A. P. Synthesis of defect perovskites $(He_{2-x}Y_x)(CaZr)F_6$ by inserting helium into the negative thermal expansion material $CaZrF_6$. *J. Am. Chem. Soc.* **139**, 13284–13287 (2017).
125. De, I., Desai, V. P. & Chakravarty, A. S. Magnetic properties of some complexes of Mo^{5+}. *Phys. Rev. B* **8**, 3769–3772 (1973).
126. Llorente, S. et al. Synthesis and crystal structure of $Cu^{II}Mo^{IV}F_6$ and $Cr^{II}Nb^{IV}F_6$ (LT form). *Z. Anorg. Allg. Chem.* **624**, 1538–1542 (1998).
127. Goubard, F. et al. Fluorocomplexes of niobium IV: the magnetic structure of $VNbF_6$. *J. Magn. Magn. Mater.* **146**, 129–132 (1995).
128. Yang, C. et al. Large positive thermal expansion and small band gap in double-ReO_3-type compound $NaSbF_6$. *Inorg. Chem.* **56**, 4990–4995 (2017).
129. Gupta, M. K., Singh, B., Mittal, R. & Chaplot, S. L. Negative thermal expansion behavior in ReO_3. *Phys. Rev. B* **98**, 014301 (2018).
130. Hancock, J. C. et al. Large negative thermal expansion and anomalous behavior on compression in cubic ReO_3-type $A^{II}B^{IV}F_6$: $CaZrF_6$ and $CaHfF_6$. *Chem. Mater.* **27**, 3912–3918 (2015).
131. Ticknor, J. O. et al. Zero thermal expansion and abrupt amorphization on compression in anion excess ReO_3-type cubic $YbZrF_7$. *Chem. Mater.* **30**, 3071–3077 (2018).
132. Baxter, S. J., Hester, B. R., Wright, B. R. & Wilkinson, A. P. Controlling the negative thermal expansion and response to pressure in ReO_3-type fluorides by the deliberate introduction of excess fluoride: $Mg_{1-x}Zr_{1+x}F_{6+2x}$, x = 0.15, 0.30, 0.40, and 0.50. *Chem. Mater.* **31**, 3440–3448 (2019).
133. Reddy, M., Madhavi, S., Subba Rao, G. & Chowdari, B. Metal oxyfluorides $TiOF_2$ and NbO_2F as anodes for Li-ion batteries. *J. Power Sources* **162**, 1312–1321 (2006).
134. Pérez-Flores, J. C. et al. VO_2F: a new transition metal oxyfluoride with high specific capacity for Li ion batteries. *J. Mater. Chem. A* **3**, 20508–20515 (2015).
135. Frevel, L. K. & Rinn, H. W. The crystal structure of NbO_2F and TaO_2F. *Acta Crystallogr.* **9**, 626–627 (1956).
136. Poulain, M., Lucas, J. & Tilley, R. J. A structural study of a nonstoichiometric niobium–zirconium oxyfluoride with the ReO_3 type structure. *J. Solid State Chem.* **17**, 331–337 (1976).
137. Pierce, J. W. & Vlasse, M. The crystal structures of two oxyfluorides of molybdenum. *Acta Crystallogr. B* **27**, 158–163 (1971).
138. Nakhal, S. & Lerch, M. New transition metal oxide fluorides with ReO_3-type structure. *Z. Naturforsch. B Chem. Sci.* **71**, 457–461 (2016).
139. Nakhal, S., Bredow, T. & Lerch, M. Syntheses and crystal structures of New ReO_3 type-derived transition metal oxide fluorides. *Z. Anorg. Allg. Chem.* **641**, 1036–1042 (2015).
140. Dabachi, J., Body, M., Galven, C., Boucher, F. & Legein, C. Preparation-dependent composition and O/F ordering in NbO_2F and TaO_2F. *Inorg. Chem.* **56**, 5219–5232 (2017).
141. Liu, K., Li, K., Peng, Q. & Zhang, C. A brief review on key technologies in the battery management system of electric vehicles. *Front. Mech. Eng.* **14**, 47–64 (2019).
142. Cambaz, M. A. et al. Vanadium oxyfluoride/few-layer graphene composite as a high-performance cathode material for lithium batteries. *Inorg. Chem.* **55**, 3789–3796 (2016).
143. Chen, R. et al. Lithiation-driven structural transition of VO_2F into disordered rock-salt Li_xVO_2F. *RSC Adv.* **6**, 65112–65118 (2016).
144. Wang, X. et al. Structural changes in a high-energy density VO_2F cathode upon heating and Li cycling. *ACS Appl. Mater. Interfaces* **1**, 4514–4521 (2018).
145. Mitchell, R. H., Welch, M. D. & Chakhmouradian, A. R. Nomenclature of the perovskite supergroup: a hierarchical system of classification based on crystal structure and composition. *Mineral. Mag.* **81**, 411–461 (2017).
146. Xue, X. & Kanzaki, M. High-pressure δ-$Al(OH)_3$ and δ-AlOOH phases and isostructural hydroxides/oxyhydroxides: new structural insights from high-resolution ^{1}H and ^{27}Al NMR. *J. Phys. Chem. B* **111**, 13156–13166 (2007).
147. Welch, M. D. & Kleppe, A. K. Polymorphism of the hydroxide perovskite $Ga(OH)_3$ and possible proton-driven transformational behaviour. *Phys. Chem. Miner.* **43**, 515–526 (2016).
148. Au-Yeung, S. C. F., Denes, G., Greedan, J. E., Eaton, D. R. & Birchall, T. A novel synthetic route to "iron trihydroxide, $Fe(OH)_3$": characterization and magnetic properties. *Inorg. Chem.* **23**, 1513–1517 (1984).
149. Au-Yeung, S. C. F. et al. The preparation and characterization of iron trihydroxide, $Fe(OH)_3$. *Can. J. Chem.* **63**, 3378–3385 (1985).
150. Schubert, K. & Seitz, A. Kristallstruktur von $Sc(OH)_3$ und $In(OH)_3$. *Z. Anorg. Allg. Chem.* **256**, 226–238 (1948).
151. Mullica, D., Beall, G., Milligan, W., Korp, J. & Bernal, I. The crystal structure of cubic $In(OH)_3$ by X-ray and neutron diffraction methods. *J. Inorg. Nucl. Chem. Lett.* **41**, 277–282 (1979).
152. Mullica, D. & Milligan, W. Structural refinement of cubic $Lu(OH)_3$. *J. Inorg. Nucl. Chem.* **42**, 223–227 (1980).

153. Mullica, D., Sappenfield, E., Gable, D. & Tims, T. Crystal structural analyses of 1:3 (Lu, In)$(OH)_3$ and 1:3 (Yb, In)$(OH)_3$. *J. Less-Common Met.* **152**, 157–163 (1989).
154. Birch, W. D., Pring, A., Reller, A. & Schmalle, H. Bernalite: a new ferric hydroxide with perovskite structure. *Naturwissenschaften* **79**, 509–511 (1992).
155. Li, B. et al. In_2O_3 hollow microspheres: synthesis from designed $In(OH)_3$ precursors and applications in gas sensors and photocatalysis. *Langmuir* **22**, 9380–9385 (2006).
156. Morgenstern-Badarau, I. Effet Jahn–Teller et structure cristalline de l'hydroxyde $CuSn(OH)_6$. *J. Solid State Chem.* **17**, 399–406 (1976).
157. Neilson, J. R., Kurzman, J. A., Seshadri, R. & Morse, D. E. Ordering double perovskite hydroxides by kinetically controlled aqueous hydrolysis. *Inorg. Chem.* **50**, 3003–3009 (2011).
158. Mizoguchi, H., Bhuvanesh, N. S. P., Kim, Y.-I., Ohara, S. & Woodward, P. M. Hydrothermal crystal growth and structure determination of double hydroxides $LiSb(OH)_6$, $BaSn(OH)_6$, and $SrSn(OH)_6$. *Inorg. Chem.* **53**, 10570–10577 (2014).
159. Nakayama, N., Kosuge, K., Kachi, S., Shinjo, T. & Takada, T. Magnetic properties of $FeSn(OH)_6$ and its oxidation product, $FeSnO(OH)_5$. *Mater. Res. Bull.* **13**, 17–22 (1978).
160. Xu, R., Deng, B., Min, L., Xu, H. & Zhong, S. $CuSn(OH)_6$ submicrospheres: room-temperature synthesis and weak antiferromagnetic behavior. *Mater. Lett.* **65**, 733–735 (2010).
161. Wu, J. M. & Chen, Y. N. The surface plasmon resonance effect on the enhancement of photodegradation activity by Au/$ZnSn(OH)_6$ nanocubes. *Dalton Trans.* **44**, 16294–16303 (2015).
162. Wang, L. et al. Single-crystalline $ZnSn(OH)_6$ hollow cubes via self-templated synthesis at room temperature and their photocatalytic properties. *J. Mater. Chem.* **21**, 4352 (2011).
163. Gao, Y. et al. Perovskite hydroxide $CoSn(OH)_6$ nanocubes for efficient photoreduction of CO_2 to CO. *ACS Sustain. Chem. Eng.* **6**, 781–786 (2018).
164. Chen, D. et al. Preferential cation vacancies in perovskite hydroxide for the oxygen evolution reaction. *Angew. Chem. Int. Ed.* **57**, 8691–8696 (2018).
165. Shinagawa, T., Garcia-Esparza, A. T. & Takanabe, K. Insight on Tafel slopes from microkinetic analysis of aqueous electrocatalysis for energy conversion. *Sci. Rep.* **5**, 13801 (2015).
166. Li, B.-Q. et al. Regulating *p*-block metals in perovskite nanodots for efficient electrocatalytic water oxidation. *Nat. Commun.* **8**, 934 (2017).
167. Welch, M. D., Crichton, W. A. & Ross, N. L. Compression of the perovskite-related mineral bernalite $Fe(OH)_3$ to 9 GPa and a reappraisal of its structure. *Mineral. Mag.* **69**, 309–315 (2005).
168. Oftedal, I. Die Kristallstruktur von Skutterudit und Speiskobalt-chloanthit. *Z. Kristallogr. Cryst. Mater.* **66**, 517–546 (1928).
169. Mandel, N. & Donohue, J. The refinement of the crystal structure of skutterudite, $CoAs_3$. *Acta Crystallogr. B* **27**, 2288–2289 (1971).
170. von Schnering, H. G. Homoatomic bonding of main group elements. *Angew. Chem. Int. Ed.* **20**, 33–51 (1981).
171. Jeitschko, W. & Braun, D. $LaFe_4P_{12}$ with filled $CoAs_3$-type structure and isotypic lanthanoid–transition metal polyphosphides. *Acta Crystallogr. B* **33**, 3401–3406 (1977).
172. Meisner, G. Superconductivity and magnetic order in ternary rare earth transition metal phosphides. *Phys. C.* **108**, 763–764 (1981).
173. Sales, B. C., Mandrus, D. & Williams, R. K. Filled skutterudite antimonides: a new class of thermoelectric materials. *Science* **272**, 1325–1328 (1996).
174. Caillat, T., Borshchevsky, A. & Fleurial, J. Properties of single crystalline semiconducting $CoSb_3$. *J. Appl. Phys.* **80**, 4442–4449 (1996).
175. Snyder, G. J. & Toberer, E. S. Complex thermoelectric materials. *Nat. Mater.* **7**, 105–114 (2008).
176. Gaultois, M. W. et al. Data-driven review of thermoelectric materials: performance and resource considerations. *Chem. Mater.* **25**, 2911–2920 (2013).
177. Shi, X. et al. Multiple-filled skutterudites: high thermoelectric figure of merit through separately optimizing electrical and thermal transports. *J. Am. Chem. Soc.* **133**, 7837–7846 (2011).
178. Khan, A. U. et al. Nano-micro-porous skutterudites with 100% enhancement in ZT for high performance thermoelectricity. *Nano Energy* **31**, 152–159 (2017).
179. Buser, H. J., Schwarzenbach, D., Petter, W. & Ludi, A. The crystal structure of Prussian blue: $Fe_4[Fe(CN)_6]_3.xH_2O$. *Inorg. Chem.* **16**, 2704–2710 (1977).
180. Chapman, K. W., Chupas, P. J. & Kepert, C. J. Compositional dependence of negative thermal expansion in the Prussian blue analogues $M^{II}Pt^{IV}(CN)_6$ (M = Mn, Fe, Co, Ni, Cu, Zn, Cd). *J. Am. Chem. Soc.* **128**, 7009–7014 (2006).
181. Gao, Q. et al. Low-frequency phonon driven negative thermal expansion in cubic $GaFe(CN)_6$ Prussian blue analogues. *Inorg. Chem.* **57**, 10918–10924 (2018).
182. Behera, J. N., D'Alessandro, D. M., Soheilnia, N. & Long, J. R. Synthesis and characterization of ruthenium and iron–ruthenium Prussian blue analogues. *Chem. Mater.* **21**, 1922–1926 (2009).
183. Williams, D., Pleune, B., Leinenweber, K. & Kouvetakis, J. Synthesis and structural properties of the binary framework C–N compounds of Be, Mg, Al, and Tl. *J. Solid State Chem.* **159**, 244–250 (2001).
184. Brousseau, L. C., Kouvetakis, W. D. & O'Keeffe, M. Synthetic routes to $Ga(CN)_5$ and $MGa(CN)_4$ (M = Li, Cu) framework structures. *J. Am. Chem. Soc.* **119**, 6292–6296 (1997).
185. Williams, D. J., Partin, D. E., Lincoln, F. J., Kouvetakis, J. & O'Keeffe, M. The disordered crystal structures of $Zn(CN)_2$ and $Ga(CN)_3$. *J. Solid State Chem.* **134**, 164–169 (1997).
186. Williams, D., Kouvetakis, J. & O'Keeffe, M. Synthesis of nanoporous cubic $In(CN)_3$ and $In_{1-x}Ga_x(CN)_3$ and corresponding inclusion compounds. *Inorg. Chem.* **37**, 4617–4620 (1998).
187. Shi, N. et al. Negative thermal expansion in cubic $FeFe(CN)_6$ Prussian blue analogues. *Dalton Trans.* **48**, 3658–3663 (2019).
188. Yang, J., Wang, H., Lu, L., Shi, W. & Zhang, H. Large-scale synthesis of Berlin green $Fe[Fe(CN)_6]$ microcubic crystals. *Cryst. Growth Des.* **6**, 2438–2440 (2006).
189. Gao, Q. et al. Switching between giant positive and negative thermal expansions of a $YFe(CN)_6$-based Prussian blue analogue induced by guest species. *Angew. Chem. Int. Ed.* **56**, 9023–9028 (2017).
190. Kumar, A., Yusuf, S. M. & Keller, L. Structural and magnetic properties of $Fe[Fe(CN)_6] \cdot 4H_2O$. *Phys. Rev. B* **71**, 054414 (2005).
191. Ohba, M. & O-kawa, H. Synthesis and magnetism of multi-dimensional cyanide-bridged bimetallic assemblies. *Coordin. Chem. Rev.* **198**, 313–328 (2000).
192. Ferlay, S., Mallah, T., Ouahe`s, R., Veillet, P. & Verdaguer, M. A room-temperature organometallic magnet based on Prussian blue. *Nature* **378**, 701–703 (1995).
193. Ohkoshi, S. I., Arai, K. I., Sato, Y. & Hashimoto, K. Humidity-induced magnetization and magnetic pole inversion in a cyano-bridged metal assembly. *Nat. Mater.* **3**, 857–861 (2004).
194. Lu, Y., Wang, L., Cheng, J. & Goodenough, J. B. Prussian blue: a new framework of electrode materials for sodium batteries. *Chem. Commun.* **48**, 6544 (2012).
195. Zhang, J. et al. $FeFe(CN)_6$ nanocubes as a bipolar electrode material in aqueous symmetric sodium-ion batteries. *Chem. Plus. Chem.* **82**, 1170–1173 (2017).
196. Wu, X. et al. Single-crystal $FeFe(CN)_6$ nanoparticles: a high capacity and high rate cathode for Na-ion batteries. *J. Mater. Chem. A* **1**, 10130 (2013).
197. Wu, X. et al. Low defect $FeFe(CN)_6$ framework as stable host material for high performance Li-ion batteries. *ACS Appl. Mater. Interfaces* **8**, 23706–23712 (2016).
198. Shadike, Z. et al. Long life and high-rate Berlin green $FeFe(CN)_6$ cathode material for a non-aqueous potassium-ion battery. *J. Mater. Chem. A* **5**, 6393–6398 (2017).
199. Cliffe, M. J. et al. Strongly coloured thiocyanate frameworks with perovskite-analogue structures. *Chem. Sci.* **10**, 793–801 (2019).
200. Ravnsbæk, D. B. et al. Thermal polymorphism and decomposition of $Y(BH_4)_3$. *Inorg. Chem.* **49**, 3801–3809 (2010).
201. Ley, M. B. et al. Complex hydrides for hydrogen storage-new perspectives. *Mater. Today* **17**, 122–128 (2014).
202. Mohtadi, R. & Orimo, S.-i. The renaissance of hydrides as energy materials. *Nat. Rev. Mater.* **2**, 16091 (2017).
203. Yan, Y. et al. Dehydriding and rehydriding properties of yttrium borohydride $Y(BH_4)_3$ prepared by liquid-phase synthesis. *Int. J. Hydrog. Energy* **34**, 5732–5736 (2009).
204. Olsen, J. E. et al. Structure and thermal properties of composites with RE-borohydrides (RE = La, Ce, Pr, Nd, Sm, Eu, Gd, Tb, Er, Yb or Lu) and $LiBH_4$. *RSC Adv.* **4**, 1570–1582 (2014).
205. Ley, M. B., Jørgensen, M., C˘erný, R., Filinchuk, Y. & Jensen, T. R. From $M(BH_4)_3$ (M = La, Ce) borohydride frameworks to controllable synthesis of porous hydrides and ion conductors. *Inorg. Chem.* **55**, 9748–9756 (2016).
206. GharibDoust, S. P. et al. Synthesis, structure, and polymorphic transitions of praseodymium(III) and neodymium(III) borohydride, $Pr(BH_4)_3$ and $Nd(BH_4)_3$. *Dalton Trans.* **47**, 8307–8319 (2018).
207. Grinderslev, J. B., Møller, K. T., Bremholm, M. & Jensen, T. R. Trends in synthesis, crystal structure, and thermal and magnetic properties of rare-earth metal borohydrides. *Inorg. Chem.* **58**, 5503–5517 (2019).
208. Ley, M. B. et al. $LiCe(BH_4)_3Cl$, a new lithium-ion conductor and hydrogen storage material with isolated tetranuclear anionic clusters. *Chem. Mater.* **24**, 1654–1663 (2012).
209. Latroche, M. et al. Full-cell hydride-based solid-state Li batteries for energy storage. *Int. J. Hydrog. Energy* **44**, 7875–7887 (2019).
210. Maouel, H. A., Alonzo, V., Roisnel, T., Rebbah, H. & Le Fur, E. The first three-dimensional vanadium hypophosphite. *Acta Crystallogr. A* **65**, i36–i38 (2009).
211. Evans, H. A. et al. Polymorphism in $M(H_2PO_2)_3$ (M = V, Al, Ga) compounds with the perovskite-related ReO_3 structure. *Chem. Commun.* **55**, 2964–2967 (2019).
212. Yang, W. et al. Carbon nanotube reinforced polylactide/basalt fiber composites containing aluminium hypophosphite: thermal degradation, flame retardancy and mechanical properties. *RSC Adv.* **5**, 105869–105879 (2015).
213. Bermúdez-García, J. M. et al. Giant barocaloric effect in the ferroic organic–inorganic hybrid $[TPrA][Mn(dca)_3]$ perovskite under easily accessible pressures. *Nat. Commun.* **8**, 15715 (2017).
214. Jain, P., Dalal, N. S., Toby, B. H., Kroto, H. W. & Cheetham, A. K. Order–disorder antiferroelectric phase transition in a hybrid inorganic–organic framework with the perovskite architecture. *J. Am. Chem. Soc.* **130**, 10450–10451 (2008).
215. Jain, P. et al. Multiferroic behavior associated with an order–disorder hydrogen bonding transition in metal–organic frameworks (MOFs) with the perovskite ABX_3 architecture. *J. Am. Chem. Soc.* **131**, 13625–13627 (2009).
216. Wang, Z., Hu, K., Gao, S. & Kobayashi, H. Formate-based magnetic metal–organic frameworks templated by protonated amines. *Adv. Mater.* **22**, 1526–1533 (2010).
217. Goldschmidt, V. M. Die Gesetze der Krystallochemie. *Naturwissenschaften* **14**, 477–485 (1926).
218. Kieslich, G., Sun, S. & Cheetham, A. K. Solid-state principles applied to organic–inorganic perovskites: new tricks for an old dog. *Chem. Sci.* **5**, 4712–4715 (2014).
219. Kieslich, G., Sun, S. & Cheetham, A. K. An extended tolerance factor approach for organic–inorganic perovskites. *Chem. Sci.* **6**, 3430–3433 (2015).
220. Seifert, H. On the existence of a vanadium (IV) formate. *J. Inorg. Nucl. Chem.* **27**, 1269–1270 (1965).
221. Tian, Y.-Q., Zhao, Y.-M., Xu, H.-J. & Chi, C.-Y. CO_2 template synthesis of metal formates with a ReO_3 net. *Inorg. Chem.* **46**, 1612–1616 (2007).
222. Paredes-García, V. et al. Structural and magnetic characterization of the tridimensional network $[Fe(HCO_2)_3] \cdot n HCO_2H$. *New J. Chem.* **37**, 2120 (2013).
223. Görne, A. L. et al. Ammonothermal synthesis, crystal structure, and properties of the ytterbium(II) and ytterbium(III) amides and the first two rare-earth-metal guanidinates, $YbC(NH)_3$ and $Yb(CN_3H_4)_2$. *Inorg. Chem.* **55**, 6161–6168 (2016).
224. Hu, K.-L., Kurmoo, M., Wang, Z. & Gao, S. Metal–organic perovskites: synthesis, structures, and magnetic properties of $[C(NH_2)_3][M^{II}(HCOO)_3]$ (M = Mn, Fe, Co, Ni, Cu, and Zn; $C(NH_2)_3$ = guanidinium). *Chem. Eur. J.* **15**, 12050–12064 (2009).
225. Evans, H. A. et al. Hydrogen bonding controls the structural evolution in perovskite-related hybrid platinum(IV) iodides. *Inorg. Chem.* **57**, 10375–10382 (2018).
226. Müller-Buschbaum, K. & Mokaddem, Y. Three-dimensional networks of lanthanide 1,2,4-triazolates: $[Yb(Tz)_3]$ and $[Eu_2(Tz)_5(TzH)_2]$, the first 4f networks with complete nitrogen coordination. *Chem. Commun.* **2006**, 2060–2062 (2006).

227. Rybak, J.-C., Rekawka, A. & Müller-Buschbaum, K. Utilizing a metal melt of gallium for the synthesis of the homoleptic 1,2,4-triazolate dense framework $[Ga(Tz)_3]$. *Z. Anorg. Allg. Chem.* **639**, 2382–2385 (2013).
228. Schweinefuß, M. E. et al. Indium imidazolate frameworks with differently distorted ReO_3-type structures: syntheses, structures, phase transitions, and crystallization studies. *Cryst. Growth Des.* **14**, 4664–4673 (2014).
229. Matsumoto, K. et al. A peanut-shaped polyaromatic capsule: solvent-dependent transformation and electronic properties of a non-contacted fullerene dimer. *Angew. Chem. Inter. Ed.* **58**, 8463–8467 (2019).
230. Abrahams, B. F., Hoskins, B. F., Robson, R. & Slizys, D. A. α-Polonium coordination networks constructed from bis(imidazole) ligands. *CrystEngComm* **4**, 478–482 (2002).
231. Eddaoudi, M. Systematic design of pore size and functionality in isoreticular MOFs and their application in methane storage. *Science* **295**, 469–472 (2002).
232. Yaghi, O. M. et al. Reticular synthesis and the design of new materials. *Nature* **423**, 705–714 (2003).
233. Férey, G. Hybrid porous solids: past, present, future. *Chem. Soc. Rev.* **37**, 191–214 (2008).
234. Lock, N. et al. Elucidating negative thermal expansion in MOF-5. *J. Phys. Chem. C* **114**, 16181–16186 (2010).
235. Deng, H. et al. Multiple functional groups of varying ratios in metal–organic frameworks. *Science* **327**, 846–850 (2010).
236. Kong, X. et al. Mapping of functional groups in metal–organic frameworks. *Science* **341**, 882–885 (2013).
237. Perry, J. J. IV, Perman, J. A. & Zaworotko, M. J. Design and synthesis of metal–organic frameworks using metal–organic polyhedra as supermolecular building blocks. *Chem. Soc. Rev.* **38**, 1400 (2009).
238. Li, J.-R., Timmons, D. J. & Zhou, H.-C. Interconversion between molecular polyhedra and metal–organic frameworks. *J. Am. Chem. Soc.* **131**, 6368–6369 (2009).
239. Biswas, S. et al. A cubic coordination framework constructed from benzobistrazolate ligands and zinc ions having selective gas sorption properties. *Dalton Trans.* **33**, 6487–6495 (2009).
240. Go´mez-Gualdro´n, D. A., Wilmer, C. E., Farha, O. K., Hupp, J. T. & Snurr, R. Q. Exploring the limits of methane storage and delivery in nanoporous materials. *J. Phys. Chem. C* **118**, 6941–6951 (2014).
241. Wilmer, C. E. et al. Large-scale screening of hypothetical metal–organic frameworks. *Nat. Chem.* **4**, 83–89 (2012).
242. He, J., Yu, J., Zhang, Y., Pan, Q. & Xu, R. Synthesis, structure, and luminescent property of a heterometallic metal–organic framework constructed from rod-shaped secondary building blocks. *Inorg. Chem.* **44**, 9279–9282 (2005).
243. Henke, S., Schneemann, A., Wütscher, A. & Fischer, R. A. Directing the breathing behavior of pillared-layered metal–organic frameworks via a systematic library of functionalized linkers bearing flexible substituents. *J. Am. Chem. Soc.* **134**, 9464–9474 (2012).
244. Zhu, A.-X. et al. Coordination network that reversibly switches between two nonporous polymorphs and a high surface area porous phase. *J. Am. Chem. Soc.* **140**, 15572–15576 (2018).
245. Tan, J. C. & Cheetham, A. K. Mechanical properties of hybrid inorganic–organic framework materials: establishing fundamental structure–property relationships. *Chem. Soc. Rev.* **40**, 1059–1080 (2011).
246. Nowacki, W. Die Kristallstruktur von ScF_3. *Z. Kristallogr. Cryst. Mater.* **101**, 273–283 (1939).
247. Drozdov, A. P., Eremets, M. I., Troyan, I. A., Ksenofontov, V. & Shylin, S. I. Conventional superconductivity at 203 kelvin at high pressures in the sulfur hydride system. *Nature* **525**, 73–76 (2015).
248. Duan, D. et al. Pressure-induced metallization of dense $(H_2S)_2H_2$ with high-Tc superconductivity. *Sci. Rep.* **4**, 6968 (2014).
249. Einaga, M. et al. Crystal structure of the superconducting phase of sulfur hydride. *Nat. Phys.* **12**, 835–838 (2016).
250. Gordon, E. E. et al. Structure and composition of the 200 K-superconducting phase of H_2S at ultrahigh pressure: the perovskite $(SH^-)(H_3S^+)$. *Angew. Chem. Int. Ed.* **55**, 3682–3684 (2016).
251. Majumdar, A., Tse, J. S. & Yao, Y. Mechanism for the structural transformation to the modulated superconducting phase of compressed hydrogen sulfide. *Sci. Rep.* **9**, 5023 (2019).
252. Momma, K. & Izumi, F. VESTA 3 for three-dimensional visualization of crystal, volumetric and morphology data. *J. Appl. Crystallogr.* **44**, 1272–1276 (2011).
253. Rosi, N. L., Eddaoudi, M., Kim, J., O'Keeffe, M. & Yaghi, O. M. Advances in the chemistry of metal–organic frameworks. *CrystEngComm* **4**, 401–404 (2002).

Acknowledgements

H.A.E. thanks the National Research Council (USA) for financial support through the Research Associate Program. A.K.C. thanks the Ras al Khaimah Centre for Advanced Materials for financial support. H.A.E and R.S. at UC Santa Barbara were supported by the US Department of Energy, Office of Science, Basic Energy Sciences under award number DE-SC-0012541.

Author contributions

H.A.E. wrote most of the Inorganic systems section. A.K.C. mapped out the original concept of the article and wrote the Introduction and most of the Metal–organic frameworks section. Y.W. contributed significantly to the Metal–organic frameworks section. R.S. worked extensively on the figures and captions, and provided input throughout the review.

Competing interests

The authors declare no competing interests.

Publisher's note

Springer Nature remains neutral with regard to jurisdictional claims in published maps and institutional affiliations.